

1 **Petrogenesis and tectonic setting of late Paleoproterozoic diorites in the**
2 **Trans-North China Orogen**

3

4 Zhiyi Wang ^{a,b}, Jun He ^{a*}, Wolfgang Siebel ^b, Shuhao Tang ^a, Yiru Ji ^a, Jianfeng He ^a, Fukun Chen ^a

5

6

7 a: State Key Laboratory of Lithospheric and Environmental Coevolution, School of Earth and
8 Space Sciences, University of Science and Technology of China, Hefei 230026, China

9 b: Institute of Earth and Environmental Sciences, Albert-Ludwig University Freiburg, Freiburg

10 79104, Germany

11

12

13 *Corresponding author: jhe1989@ustc.edu.cn (J. He)

14

15

16 **Abstract:** Unravelling the tectonic setting and evolution of cratons during the late
17 Paleoproterozoic has long been a major focus of geological research. As one of Earth's
18 principal cratonic blocks, the North China Craton (NCC) preserves extensive
19 magmatism during this period. Recent investigations have identified numerous 1.78
20 Ga dioritic intrusions along the southern margin and the center of the NCC. The NCC
21 experienced a widespread magmatic event at 1.78 Ga, and the tectonic setting of this
22 period remains a central and actively debated topic, demanding further interpretation
23 and understanding. Diorites of the NCC provide critical petrogenetic and geological
24 significances. In this paper we report zircon U-Pb ages of ~1.78 Ga and geochemical
25 data of the Jiguanshan diorite. The diorites in the Trans-North China Orogen and the
26 southern margin of the NCC, including the Jiguanshan diorite, have similar element
27 and isotopic characteristics. The weighted mean average of initial $^{87}\text{Sr}/^{86}\text{Sr}$ and $\epsilon_{\text{Nd}}(t)$
28 values is 0.7052 ± 0.0003 and -6.5 ± 0.2 , respectively. The initial Pb isotope
29 compositions of the diorite samples do not show significant enrichment of radiogenic
30 lead. In terms of Sr-Nd-Pb isotope compositions and Nb/Ta, Ba/Th, and Sr/Th ratios,
31 the diorites differ from the coeval Xiong'er volcanic rocks and mafic dike swarms.
32 Our results suggest that the diorites originated from the basaltic lower crust, rather
33 than from the enriched subcontinental lithospheric mantle. Whole-rock and zircon
34 trace element tectonic diagrams indicate that the diorites formed in a rift-related
35 environment. The formation of the diorites indicates a potential transition from
36 orogenic-related magmatism towards intraplate magmatism.

37 **Key words:** Late Paleoproterozoic, North China, Diorite, Zircon, Sr-Nd-Pb isotopes

删除的内容:

删除的内容: The Xiong'er volcanic rocks and mafic dike swarms mark a significant magmatic event after the amalgamation of the North China Craton (NCC) in the Paleoproterozoic, yet their tectonic origins remain controversial. Several Paleoproterozoic diorite intrusions have received widespread attention recently. Their genesis and geological significance are crucial for understanding the evolution of the NCC. In this study, we

删除的内容: se

删除的内容: Whole-rock and zircon trace element geological tectonic diagrams indicate that the diorites formed in a rift environment. These diorites mark a crustal-origin rock shift from orogenic-related magmatism to intraplate magmatism during the post-collisional extensional stage.

删除的内容: .

62 **1 Introduction**

63 Formation and evolution of the North China Craton (NCC) provide critical insights
64 into Precambrian Earth processes (e.g., Geng et al., 2012; Liu et al., 1992). The NCC
65 was stabilized by the collision and amalgamation of continental blocks in the late
66 Paleoproterozoic (Fig. 1a; e.g., Zhao and Zhai, 2013; Zhao et al., 2000a, b).
67 Subsequent widespread magmatic activity across the NCC recorded the cratonization
68 process, providing critical insights into its stabilization and maturation (e.g., Zhai,
69 2011). The petrogenesis of these Paleoproterozoic magmatic rocks preserves key
70 information about regional tectonic evolution and has been linked to the assembly or
71 breakup of Columbia supercontinents (e.g., Peng et al., 2007, 2008; Zhao et al., 2009).
72 Among these events, the ~1.78 Ga magmatism is particularly distinctive due to its
73 large scale, producing numerous rock types including the Xiong'er Group, A-type
74 granite and mafic dykes (e.g., Cui et al., 2010; Hu et al., 2010; Peng et al., 2007, 2008;
75 Wang et al., 2004; Wang et al., 2014). These rocks are extensively distributed across
76 both the southern margin and Trans-North China Orogen of the NCC. However, the
77 petrogenesis and tectonic setting of these rocks is controversially debated, which
78 revolves around post-collisional/orogenic extension (e.g., Wang et al., 2004, 2008
79 2014), continental arc magmatism (e.g., He et al., 2009; Zhao et al., 2009), rifting
80 (e.g., Cui et al., 2010; Zhao et al., 2007), and the involvement of mantle plumes (e.g.,
81 Hou et al., 2008; Peng et al., 2007, 2008). Clarifying the tectonic setting during this
82 period is essential for understanding evolution that followed the late Paleoproterozoic
83 amalgamation of the NCC.

84 In recent years, numerous diorites with ages of c. 1780 Ma along the southern margin
85 of the NCC and the Shanxi region (Fig. 1b) have attracted significant attention,
86 potentially offering new perspectives for understanding the tectonic evolution of the

已移动(插入) [1]

已移动(插入) [2]

带格式的: 字体颜色: 自定义颜色
(RGB(0,0,204))

删除的内容: The ancient basement rocks in the North China Craton (NCC) provide crucial insights into the Precambrian geological evolution

已上移 [1]: (e.g., Geng et al., 2012; Liu et al., 1992)

删除的内容: . The main assembly of the NCC took place after the collision of eastern and western land masses in the late Paleoproterozoic

已上移 [2]: (e.g., Zhao and Zhai, 2013; Zhao et al., 2000a, b)

删除的内容: . Subsequently, the craton experienced multiple rift phases, with the Xiong'er rift being the first rift formed after the assembly, resulting in the formation of the c. 1780 Ma Xiong'er volcanic rocks and contemporaneous mafic dyke swarms (e.g., Hou et al., 2008; Peng et al., 2007, 2008; Zhai, 2010). However, the origin and tectonic setting of the Xiong'er volcanic rocks and contemporaneous mafic dyke swarms of the NCC remains controversial. The debate mainly revolves around subduction (e.g., He et al., 2009; Wang et al., 2004; Zhao et al., 2009), rifting (e.g., Cui et al., 2010; Zhao et al., 2007), and the involvement of mantle plumes (e.g., Hou et al., 2008; Peng et al., 2007, 2008). Clarifying the tectonic setting during this period is essential for understanding the post-collisional orogenic evolution that followed the late Paleoproterozoic amalgamation of the North China Craton. .

删除的内容: In recent years, numerous c. 1780 Ma diorites along the southern margin of the NCC and the Shanxi region

删除的内容: 1a

130 craton during the late Paleoproterozoic. These rocks include the diorites intruding into
131 the Xushan Formation ($c.$ 1789 Ma; Zhao et al., 2004), the East-West Group dykes ($c.$
132 1780 Ma; Peng et al., 2007), the Shizhaigou diorite ($c.$ 1780 Ma; Cui et al., 2011), the
133 Wafang diorite ($c.$ 1750 Ma; Wang et al., 2016), the Gushicun diorite ($c.$ 1780 Ma; Ma
134 et al., 2023a), the Muzhijie diorite ($c.$ 1780 Ma; Ma et al., 2023b), the Fudian diorite
135 ($c.$ 1780 Ma; Ma et al., 2023b), and the Jiguanshan diorite ($c.$ 1780 Ma; this study).
136 The diorites are widely distributed in an approximate east-west trending belt and
137 possess similar zircon ages. Peng et al. (2007) and Cui et al. (2011) proposed that
138 some of them share identical source with the Xiong'er Group volcanic rocks or dyke
139 swarms, formed by fractional crystallization of enriched mantle material. Others
140 authors interpret some of them resulting from the fractional crystallization (Ma et al.,
141 2023a, b) or from crustal melting with limited mantle influence (Wang et al., 2016).
142 Systematic research into their genesis is crucial for clarifying their formation and
143 constraining regional geological evolution.

144 The present study focuses on the Jiguanshan diorite and other diorites with ages
145 between 1.78 and 1.75 Ga from the NCC. These diorites have similar geochemical
146 characteristics, suggesting their formation during a single magmatic episode. By
147 evaluating whole rock geochemical and Sr-Nd-Pb isotopic compositions, as well as
148 Hf isotopic compositions of zircons, a better understanding of the tectonic
149 environment and evolution of the NCC during the late Paleoproterozoic is provided.

150

151 **2 Geological background and sample material**

152 The NCC records a 3.8 Ga lasting geological evolution (e.g., Geng et al., 2012; Liu et
153 al., 1992). It consists of an Archean to Paleoproterozoic metamorphic basement
154 overlain by Mesoproterozoic unmetamorphosed sedimentary cover (e.g., Lu et al.,

179 2008; Zhao and Zhai, 2013). The crystalline basement is composed of several
180 microcontinental blocks (Fig. 1a; Zhao et al., 2005). Between 1.95 and 1.92 Ga, the
181 Yinshan and Ordos blocks collided along the Khondalite belt to form the Western
182 Block (e.g., Li et al., 2011; Lu et al., 2008; Zhao et al., 2005). Around 1.9 Ga, the
183 Longgang and Nangrim blocks amalgamated along the Jiao-Liao-Ji belt, forming the
184 Eastern Block (e.g., Luo et al., 2004; Zhao et al., 2005). The NCC ultimately formed
185 by the assembly of the eastern and western blocks along the central orogenic belt at c.
186 1.85 Ga (e.g., Zhao and Zhai, 2013; Zhao et al., 2000a, b, 2005). The southern
187 margin of the NCC is separated from the North Qinling Orogen by the Luonan–
188 Luanchuan Fault (Fig. 1b). Prior to the Mesozoic, the southern margin of the NCC
189 experienced a similar geological evolution as the NCC itself, which makes it an ideal
190 object for studying the Precambrian geological evolution (e.g., Zhai, 2010).

191 The study area is located within the eastern part of the southern margin of the NCC
192 (Fig. 1b). The most frequent basement rocks in this area are metamorphic basement
193 rocks of the Archean Taihua Group. The Taihua Group extends in an east-west
194 direction from Lantian in the west to Wuyang in the east (e.g., Diwu et al., 2014, 2018;
195 Wang et al., 2020). It is primarily composed of medium- to high-grade metamorphic
196 rocks and has been divided into the Lower Taihua Complex and the Upper Taihua
197 Complex (e.g., Kröner et al., 1988; Shen, 1994; Wan et al., 2006; Xue et al., 1995;
198 Zhang et al., 1985). The lower part is dominated by metamorphic mafic rocks and
199 TTG gneisses (e.g., Kröner et al., 1988; Zhang et al., 1985). The upper part is
200 characterized by supracrustal sequences and metamorphic mafic rocks (e.g., Wan et
201 al., 2006; Xue et al., 1995). During the Archean, the rocks of the Taihua Group record
202 two significant stages of crustal growth (e.g., Diwu et al., 2014, 2018). During the
203 late Paleoproterozoic (1.97 – 1.80 Ga), the Taihua Group underwent widespread

带格式的: 字体颜色: 自定义颜色 (RGB(0,0,204))

带格式的: 字体颜色: 自定义颜色 (RGB(0,0,204))

删除的内容: It was ultimately formed by the assembly of the eastern and western blocks along the central orogenic belt at the end of the Paleoproterozoic

删除的内容: mainly occupied by the “Xiong’er rift”, which is

删除的内容: fault

删除的内容: Before the Mesozoic,

删除的内容: in

214 amphibolite to granulite facies metamorphism and intense deformation, reflecting
215 collisional orogenic events in the NCC (Diwu et al., 2018; Sun et al., 2017).

216 The upper part of the basement contains 1780 million years old volcanic rocks Xiong'
217 er Group (e.g., Zhao et al., 2004, 2007). The Xiong'er volcanic rocks consist mainly
218 of basalts and andesites that are widely distributed along the southern margin of the
219 NCC, and extend as far north as Taiyuan City in Shanxi Province (Zhao et al., 2007).
220 The Xiong'er Group represents the largest magmatic unit of the NCC since the
221 Neoarchean period. At the same time, a large mafic dyke swarm emplaced the NCC.
222 These mafic rocks are interpreted as products of crustal extension during the
223 Colombia supercontinent era (e.g., Peng et al., 2008; Wang et al., 2004).

224 During fieldwork, seven diorite samples were collected from the Jiguanshan diorite on
225 the eastern side of the Jiguanshan Hill (or the Jiguan Mountain), about 30 km south of
226 Ruyang County, Henan Province (Fig. 1c and Table S1). The Jiguanshan diorite forms
227 several east-west striking bodies that are cut by the Mesozoic Taishanmiao A-type
228 granite to the west. The Taishanmiao intrusion, located at the southern margin of the
229 NCC in the western Henan region, covers an area of c. 290 km² (e.g., He et al., 2021).

230 The northern and eastern part of the Taishanmiao intrusion penetrates the volcanic
231 rocks of the Xiong'er Group (Fig. 1c).

232 The collected rock samples of the Jiguanshan diorite are fresh and greyish with
233 massive textures (Fig. 2a). They are fine-grained with a particle size of 0.1–2 mm (Fig.
234 2b). The main mineral is plagioclase (~60 vol.%), with lamellar and euhedral shape
235 and variable grain size. Under the microscope, the partially sericitized crystals show
236 simple contact twinning and polysynthetic twinning. Some plagioclase crystals show
237 zonal and resorption textures (Figs. 2c-e) and the Carlsbad-albite twinning with zoned

删除的内容: The upper part of the basement contains volcanic rocks of the Xiong'er Group that formed ca. 1780 Ma

删除的内容: our

删除的内容: a

删除的内容: The northern and eastern part of the Taishanmiao intrusion penetrates the volcanic rocks of the Xiong'er Group

删除的内容: structures

删除的内容: a,

删除的内容: which varies greatly in size and has a lamellar and euhedral shape

删除的内容: Albite

254 | texture (Fig. 2d). Clinopyroxene (~15 vol.%) formed earlier than plagioclase. Most of
255 | the clinopyroxenes have zonal and resorption textures (Fig. 2f). Euhedral opaque
256 | minerals (~3 vol.%), such as ilmenite, are often encased in clinopyroxene.
257 | Alkaline-feldspar (~10 vol.%) shows hypidiomorphic to xenomorphic texture with
258 | imprints of kaolinization (Figs. 2c, e). The mineral occurs as K-feldspar and perthite.
259 | Quartz (~5 vol.%) occurs as an anhedral crystal. Biotite (~3 vol.%) shows
260 | xenomorphic texture or is altered into chloride (Figs. 2c, e). In addition, accessory
261 | minerals such as zircon and ilmenite account for about 3 vol.% (Fig. 2f).

删除的内容: composite twin with zoned texture

262 |
263 | **3 Analytical methods**
264 | **Major and trace elements:** Seven representative fresh rock samples were grinded
265 | into powders less than 200 mesh. Major element composition of whole rock was
266 | obtained by X-ray fluorescence (XRF) from ALS Chemex (Guangzhou) using a
267 | PANalytical PW2424 instrument. Following sample digestion, whole-rock trace
268 | element concentrations were determined using an Agilent 7700 inductively coupled
269 | plasma mass spectrometry (ICP-MS) at the University of Science and Technology of
270 | China (USTC). Quality control assurance was achieved by using GSR-1, BCR-2, and
271 | AGV-2 standard material. The analytical uncertainties are <5%.

删除的内容: -

删除的内容: Method

272 | **Whole-rock Sr-Nd-Pb isotopes:** Whole-rock Sr-Nd-Pb isotope analysis was
273 | performed in the ultra-clean laboratory of the Laboratory of Radiogenic Isotope
274 | Geochemistry, USTC. Whole-rock powders of c. 100 mg were weighed in 7 ml Teflon
275 | cups in a solution of purified HF and HNO₃ acids for Pb isotopic analysis and in a
276 | solution of purified HF and HClO₄ acids for Sr-Nd isotopic analysis. Sr and Nd were
277 | separated by AG 50W-X12 resin in 200–400 mesh purposes and purified using the

删除的内容: selected to be broken up into

删除的内容: the

删除的内容: Chemical separation of

删除的内容: w

290 Sr-Spec® ion-exchange resin for Sr and Ln-Spec® resin for Nd. All isotopic
291 measurements were done on a Triton Plus mass spectrometer of Thermo Scientific™.
292 Measured Sr and Nd ratios were normalized to $^{86}\text{Sr}/^{88}\text{Sr} = 0.1194$ and $^{143}\text{Nd}/^{144}\text{Nd} =$
293 0.7219, respectively. Pb isotope ratios were corrected for mass fractionation using a
294 fractionation factor of 0.1% per atomic mass unit based on repeated measurements of
295 reference material NIST NBS 981 (Wang et al., 2023b). Total procedure blanks for Sr,
296 Nd, and Pb were <200 pg. Description of detailed analytical procedures can be found
297 elsewhere (Chen et al., 2000, 2007). Errors of the initial values of Sr and Nd isotopes
298 were obtained by the error transfer formula, which is shown in Table 2 for Sr and
299 Table 3 for Nd. Detailed formulas can be found in Siebel et al. (2005). A 5% age error,
300 a 2‰ $^{87}\text{Rb}/^{86}\text{Sr}$ measurement error, and a 0.3‰ $^{87}\text{Sr}/^{86}\text{Sr}$ measurement error were
301 used for the error of initial Sr values for calculation. A 5% age error, a 0.3‰
302 $^{147}\text{Sm}/^{143}\text{Nd}$ error, and the $^{143}\text{Nd}/^{144}\text{Nd}$ measurement error were used for the
303 calculation of the error of initial Nd isotope values.

304 **Zircon U-Pb geochronology and trace element composition:** Zircon crystals were
305 isolated from the rocks by standard mineral separation procedures. Grains with intact
306 crystal shape and no obvious inclusions were selected under a binocular microscope.
307 The zircons were embedded in epoxy resin. The upper and lower planes of each
308 zircon target were polished with sandpaper from coarse to fine. Most of the zircon
309 gains were polished to 2/3 of the position and then cleaned in ultra-pure water by
310 ultrasonic waves. The grains were cleaned with dust-free paper in a certain direction
311 to ensure that the zircon was clean and bright without impurities under the microscope
312 for carbon plating. Cathodoluminescence (CL) image analysis was done on a scanning
313 electron microscope (SEM) located at the USTC. Zircon U-Pb isotopic and trace
314 element compositions were obtained by laser-ablation inductively-coupled plasma

删除的内容: 2023a

删除的内容: Detailed

删除的内容: The errors

删除的内容: Zircon U-Pb age and trace elements

删除的内容: without impurities under the

322 mass spectrometry (LA-ICP-MS) using an Agilent 7700 ICP-MS with a 193 nm ArF
323 laser-ablation system at the USTC. The beam spot diameter was 32 μm , operating at a
324 repetition rate of 10 Hz. Helium served as the carrier gas. Zircon 91500 was used as a
325 standard for age calculation. The NIST SRM 610 and 612 were utilized as reference
326 materials for element content adjustment. U-Pb ratios and uranium and lead
327 concentration data were calculated by the ICPMSDataCal software (Liu et al., 2010).
328 Concordia and weighted mean age plots were made using IsoplotR (Vermeesch,
329 2018).

330

331 **4 Analytical results**

332 Whole-rock compositions of the Jiguanshan diorite are given in Table 1, and
333 Sr-Nd-Pb isotope compositions and error calculations are shown in Tables 2 to 4. Age
334 results of zircon grains from four samples are given in Table S1, and trace element
335 composition in Table S2.

删除的内容: elemental contents

336

337 **4.1 Zircon U-Pb isotopic ages**

338 Zircon grains from the Jiguanshan diorite are transparent to pale yellow with
339 subhedral to euhedral habitus. They measure $c.$ 100–300 μm in length and have aspect
340 ratios of 1:1 to 3:1. Most of them show oscillatory zoning in the CL images (Fig. 3),
341 which suggests their magmatic origin.

342 Twenty-nine zircon grains from sample ZY2202 yield $^{207}\text{Pb}/^{206}\text{Pb}$ ages varying from
343 1885 ± 44 Ma to 1643 ± 42 Ma and giving a weighted mean age of 1772 ± 16 Ma (2σ ,
344 $n=29$, MSWD=2.2, Fig. 4a). Thirty-two zircon grains from sample ZY2204 yield
345 $^{207}\text{Pb}/^{206}\text{Pb}$ ages varying from 1902 ± 54 Ma to 1635 ± 47 Ma with a weighted mean

删除的内容: a

删除的内容:

带格式的: 上标

带格式的: 上标

删除的内容: One zircon has a $^{207}\text{Pb}/^{206}\text{Pb}$ age of 1639 \pm 46 Ma (96% concordance), which is excluded from the calculation

348 | age of 1742 ± 15 Ma (2σ , n=32, MSWD=1.6, Fig. 4b). Twenty-six out of twenty-seven
349 | zircon grains from sample ZY2205 yield $^{207}\text{Pb}/^{206}\text{Pb}$ ages varying from 1933 ± 52 Ma
350 | to 1692 ± 44 Ma and a weighted mean age of 1760 ± 18 Ma (2σ , n=26, MSWD=0.66,
351 | Fig. 4c). One zircon with a $^{207}\text{Pb}/^{206}\text{Pb}$ age of 1639 \pm 46 Ma (96% concordance) was
352 | excluded from the calculation (Fig. 4c). Thirty zircon grains of sample ZY2207 yield
353 | $^{207}\text{Pb}/^{206}\text{Pb}$ ages ranging from 1900 ± 54 Ma to 1700 ± 36 Ma with a weighted mean
354 | age of 1771 ± 17 Ma (2σ , n=30, MSWD=1, Fig. 4d).

355 | Most zircon grains have Th/U ratios >1 , supporting their magmatic origin (Table S1).
356 | Some grains deviate from the concordant line, which is related to lead loss (Fig. 4a-d).
357 | The weighted mean ages of the Jiguanshan diorite near 1780 Ma suggest that the
358 | diorite body formed in the late Paleoproterozoic.

359

360 4.2 Whole-rock chemical composition

361 | SiO₂ contents of the Jiguanshan diorite vary between 55.57 wt. % and 59.44 wt. %
362 | and the sum of K₂O+Na₂O from 5.57 wt. % to 6.03 wt. %, corresponding to gabbroic
363 | diorite to diorite composition according to the TAS diagram (Fig. 5a). K₂O contents
364 | range from 2.97 wt. % to 3.21 wt. % and fall within the high-K calc-alkaline fields
365 | (Fig. 5b). The samples from the Jiguanshan diorite have consistent A/CNK ratios
366 | ranging from 0.78 to 0.81 and A/NK >1 , which classify them as metaluminous rocks
367 | (Fig. 5c). Mg[#] ($\text{Mg}^{\#} = (\text{MgO} + \text{FeO}_{\text{total}})/\text{MgO} \times 100$) values range from 34 to 39 (Fig. 5d).
368 | The Jiguanshan diorite depicts the enrichment of large ion lithophile elements (LILE),
369 | such as Rb, Ba, and K, and negative anomalies of Sr, Ti, Nb, and Ta (Fig. 6a). ΣREE
370 | contents range from 361 to 393 ppm. Light rare earth elements (LREE) exhibit
371 | stronger enrichment, while heavy rare earth elements (HREE) are relatively depleted

删除的内容: The

删除的内容: ppm

删除的内容: Their

379 | (Fig. 6b). $(La/Yb)_N$ ratios range from 12.2 to 15.0 (subscript N denotes normalization
380 | against chondrite La and Yb contents) with Eu/Eu^* ($Eu/Eu^* = 2Eu_N/(Sm_N + Gd_N)$,
381 | subscript N denotes normalization against chondrite Sm and Gd contents) ratios
382 | ranging from 0.57 to 0.68 (Table 1).

383

384 4.3 Whole-rock Sr-Nd-Pb isotopic compositions

385 All initial radiogenic isotopic values and the errors of the initial values of Sr, Nd and

删除的内容: are

386 | Pb isotopes reported herein are, calculated back to an age of 1780 Ma. The measured

删除的内容: isotope compositions

387 | $^{87}Sr/^{86}Sr$ ratios of the Jiguanshan diorite vary from 0.715177 ± 0.000011 to 0.724714
388 | ± 0.000012 (2σ). Initial Sr ratios range from 0.7020 ± 0.0007 to 0.7058 ± 0.0010 (2σ ,

删除的内容: samples

389 | Fig. 7a). Measured $^{143}Nd/^{144}Nd$ values vary from 0.511129 ± 0.000008 to 0.511329

390 | ± 0.000007 (2σ). Initial $^{143}Nd/^{144}Nd$ isotope compositions range from 0.509924

391 | ± 0.000061 to 0.510090 ± 0.000063 (2σ), corresponding to initial ϵ_{Nd} values of -8.04

392 | ± 1.20 to -4.80 ± 1.23 (2σ , Fig. 7b) and two-stage Nd model ages (T_{DM2}) of 2.94 Ga to

删除的内容: Their

393 | 2.68 Ga. Pb isotopic compositions are as follows: $^{206}Pb/^{204}Pb = 15.832\text{--}16.167$,

394 | $^{207}Pb/^{204}Pb = 15.170\text{--}15.243$, and $^{208}Pb/^{204}Pb = 36.046\text{--}37.324$. Initial Pb isotope

395 | ratios are significantly lower: $^{206}Pb/^{204}Pb_i$ ratios ranging from 14.965 to 15.295,

396 | $^{207}Pb/^{204}Pb_i$ ratios ranging from 15.090 to 15.150, $^{208}Pb/^{204}Pb_i$ ratios ranging from

397 | 34.398 to 35.825, with $^{238}U/^{204}Pb$ and $^{232}Th/^{238}U$ ratios ranging from 2.3 to 2.9 and 5.3

398 | to 7.8, respectively (Fig. 8a, b).

399

400 5 Discussion

401 5.1 Compositional characteristics of late-Paleoproterozoic diorites of the NCC

402 | The late Paleoproterozoic diorites in the NCC have uniform east-west (EW) strike

408 direction, different from the north-northwest (NNW) strike of most contemporaneous
409 mafic dykes (Hou et al., 2008; Peng et al., 2007, 2008). Intrusion ages of the diorites
410 are concentrated between 1780 and 1750 Ma. All the diorites have similar
411 geochemical and isotopic compositions and can be regarded as a compositional
412 homogeneous rock group.

删除的内容: suggesting a possible correlation, which differs from the north-northwest (NNW) strike of most contemporaneous mafic dyke

删除的内容: The i

删除的内容: se

413 Most of the late-Paleoproterozoic diorites of the NCC have silica contents in the range
414 of 52 wt. % to 62 wt. % (Fig. 5a). Total alkali content (K₂O+Na₂O) of 5 wt. % to 7
415 wt. % suggests a subalkaline character (Fig. 5a). K₂O contents range from 2 wt. % to
416 5 wt. % in accordance with a high-K calc-alkaline to shoshonite composition (Fig. 5b).
417 The ASI and Mg[#] values of the samples, except for a few data points that deviate
418 significantly, are mostly homogeneous, with weighted average values of 0.81 and 37,
419 respectively (Fig. 5c, d). In primitive mantle normalization diagrams, all diorites
420 display enrichment of LILEs, such as Rb, Ba, and K, and depletion of high field
421 strength elements (HFSEs), such as Na, Ta, Th, U, and Ti (Fig. 6). On the rare earth
422 element normalization diagrams, they display negative Eu anomalies with enrichment
423 in LREEs and flat distribution of HREEs (Fig. 6).

删除的内容: Summarizing the late-Paleoproterozoic diorites of the NCC, most of them have SiO₂ contents in the range of 52–62 wt. %

删除的内容: -

删除的内容: for the diorite rocks

删除的内容: The

删除的内容: K₂O contents of these samples range from 2–5 wt. % in accordance with a high-K calc-alkaline to shoshonite series

删除的内容: se

删除的内容: On primitive mantle normalization diagrams,

删除的内容: the

删除的内容: large ion lithophilic elements (LILEs)

带格式的: 字体颜色: 自定义颜色 (RGB(0,0,204))

删除的内容: they have negative Eu anomalies with enrichment in LREEs and flat distribution of HREEs (Fig. 6). As can be seen from the above, the oxides and trace elements of these diorites have similarities. .

删除的内容: when we recalculate the initial ε_{Nd} values and their errors back to 1780 Ma using the data from previous studies

删除的内容: namely Muzhijie diorite in some literatures,

删除的内容: may

删除的内容: contents

删除的内容: late Paleoproterozoic

424 All diorites have similar Nd isotopic compositions with the mean initial ε_{Nd} value of
425 -6.51 ±0.2 (2σ, n=41, Fig. 7b), when calculate back to 1780 Ma (Table 3). The overall
426 range of initial ε_{Nd} values is from -10.2 ±1.21 to -4.80 ±1.23 (2σ, Fig. 7b). Some
427 samples from Wafang diorite (or Muzhijie diorite, Ma et al., 2023b; Wang et al., 2016)
428 have enriched Nd isotope composition, which can be explained by assimilation or
429 contamination of the continental crust due to their higher zirconium (Fig. 7b; Table 3).
430 Overall, the initial ε_{Nd} values and the corresponding two-stage Nd model ages (T_{DM2})
431 of the diorites are consistent with each other except for the Wafang diorite (Table 3).
432 The initial ε_{Hf} values of zircons from the diorites in the NCC have a wide but

471 consistent range of variations, i.e., from -17 to -2.5 in the Gushicun diorite (Ma et al.,
472 2023a; Fig. 7c), from -14 to 0.55 in the Muzhijie diorite (Ma et al., 2023b; Fig. 7c),
473 and from -17 to 0.95 in the Fudian diorite (Ma et al., 2023b; Fig. 7c). The diorites
474 have similar Nd-Hf isotopic compositions and form a coherent group in geochemical
475 diagrams, indicating a close genetic relationship.

删除的内容: :

删除的内容: In summary, t

删除的内容: he diorites in the NCC
have similar Nd-Hf isotopic
compositions and form a coherent
group in geochemical diagrams,
indicating a close genetic relationship.

477 5.2 Initial Sr isotope composition and magma source

478 The late Paleoproterozoic diorites in the NCC show a large range in whole-rock initial
479 Sr isotopic compositions (Fig. 7a; Jiguanshan diorite: 0.7020 to 0.7058; Wafang
480 diorite: 0.7004 to 0.7050; Shizhaigou diorite: 0.7005 to 0.7053; East-West group dikes:
481 0.7011 to 0.7053). Determining magma sources for rocks with widely varying initial
482 Sr ratios is complex, as Sr isotopes can be affected by magma mixing, assimilation,
483 contamination, and melting degrees. (e.g., Gao et al., 2015; Wolf et al., 2019; Zeng et
484 al., 2005).

485 The whole-rock Nd isotopic compositions of the diorites suggest a heterogeneous
486 magma source (Fig. 7b). It might be argued that this could be the effect of mixing
487 between crustal and mantle sources. However, mantle-derived rocks often have a high
488 MgO content and elevated compatible elements concentrations such as Ni and Cr,
489 which is inconsistent with the elemental content characteristics of the diorites (Table 1,
490 see previous references). Variability in Sr isotopic compositions can result from
491 different degrees of source melting. However, a mica- and feldspar-rich source with
492 high Rb/Sr ratios produces melts with more radiogenic $^{87}\text{Sr}/^{86}\text{Sr}$ ratios (e.g., Hu et al.,
493 2018). Melts affected by the dehydration of amphibole typically have low $^{87}\text{Sr}/^{86}\text{Sr}$
494 ratios with adakitic characteristics (e.g., Rapp and Watson, 1995; Wolf et al., 1993).

删除的内容: without mixing with the
mantle

删除的内容: On the other hand, m

删除的内容: levels of

删除的内容: are

删除的内容: es

删除的内容: .

495 The different degrees of source melting are unlikely to be the main cause for the

510 isotopic composition of the diorites,

511 Initial $^{87}\text{Sr}/^{86}\text{Sr}$ values <0.704 are negatively correlated with the $^{87}\text{Rb}/^{86}\text{Sr}$ ratios (Fig.

512 7a). For initial $^{87}\text{Sr}/^{86}\text{Sr}$ values >0.704 , such correlation no longer exists. A reason

513 for this could be the large uncertainty propagation of the initial whole-rock Sr isotope

514 ratios especially for old samples. All diorites have samples with the initial $^{87}\text{Sr}/^{86}\text{Sr}$

515 values greater than 0.704. Excluding outliers, the mean average initial $^{87}\text{Sr}/^{86}\text{Sr}$ value

516 is 0.7052 ± 0.0003 (2σ , $n=8$), which might represent the most likely initial Sr isotopic

517 composition of the source (Fig. 7a).

删除的内容: The different degrees of source melting are unlikely to be the main cause.

删除的内容: The initial $^{87}\text{Sr}/^{86}\text{Sr}$ values negatively correlate with the $^{87}\text{Rb}/^{86}\text{Sr}$ ratios when they are less than 0.704

删除的内容: When the

删除的内容: initial $^{87}\text{Sr}/^{86}\text{Sr}$ values are greater than 0.704,

删除的内容: The

删除的内容: large uncertainty propagation in calculating the initial whole-rock Sr isotope compositions for old samples may be the main factor

518 The initial Sr ratios of the Xiong'er Group rocks vary widely and tend to be more

519 radiogenic (Fig. 7d). The initial Sr ratios of these diorites are more similar to lower

520 crustal Archean xenoliths from the southeastern NCC (initial $^{87}\text{Sr}/^{86}\text{Sr}$ values: 0.7039–

521 0.7068, $t=1780$ Ma, e.g., Huang et al., 2004), suggesting that they are more likely

522 associated with lower crustal rocks of the NCC rather than an enriched mantle source

523 like the volcanic rocks of the Xiong'er Group.

删除的内容: The initial Sr isotopic compositions of the Xiong'er Group rocks vary widely and tend to have more variable and radiogenic Sr isotopic ratios

删除的内容: i

删除的内容: isotope compositions

删除的内容: much

删除的内容: the

删除的内容: in

524

5.3 Petrogenetic considerations

526 Several models have been proposed for the petrogenesis of intermediate dioritic rocks

527 including partial melting of metasomatized mantle (e.g., Chen et al., 2021), partial

528 melting of subducted oceanic crust and subsequent melt-peridotite reaction (e.g.,

529 Kelemen, 1995; Stern and Kilian, 1996), magma mixing/mingling (e.g., Reubi and

530 Blundy, 2009; Streck et al., 2007), melting of basaltic rocks (e.g., Jackson et al., 2003;

531 Petford and Atherton, 1996), as well as fractional crystallization of basaltic magmas

532 (e.g., Castillo et al., 1999).

删除的内容: hypotheses

533 The diorites from the NCC have low compatible element concentrations, suggesting

560 that they were not derived directly from a mantle source (Fig. 9a). Larger contribution
561 of mantle material can also be excluded due to their relatively homogeneous initial Nd
562 isotope compositions (Fig. 7b), and consistent silica and Mg[#] values (Fig. 5d).

563 Partial melting of the oceanic crust in the subducted slab can also form rocks of
564 intermediate composition, such as adakites, which often exhibit high Sr/Y ratios (>20)
565 and low Y contents (<18 ppm) (e.g., Defant and Drummond, 1990; Peacock et al.,
566 1994). The Jiguanshan and other diorites from the NCC have relatively high Y and Sr
567 contents with Sr/Y ratios <15. Thus, partial melting of the oceanic crust does not

568 appear to have played a role during the genesis of the diorites,

569 As can be seen from the Harker variation diagrams, the Cr contents decrease with
570 decreasing MgO, indicating fractionation of clinopyroxene (Fig. 9a). CaO contents
571 decrease with increasing SiO₂, suggesting crystallization of minerals, such as
572 plagioclase or clinopyroxene (Fig. 9b). However, Al₂O₃ and Na₂O contents do not
573 significantly decrease with increasing SiO₂, indicating that plagioclase and
574 clinopyroxene were not significant fractionation phases (Figs. 9c-d). The increase in
575 K₂O contents with increasing SiO₂ suggests no biotite and/or K-feldspar fractionation
576 during magmatic evolution (Fig. 9e). The increasing SiO₂ and decreasing TiO₂
577 indicate the crystallization and fractionation of Ti-bearing minerals, such as ilmenite
578 (Fig. 9f). The Eu/Eu^{*} values of the diorites do not show significant changes with Sr

579 contents, which proves that fractionation of plagioclase from the melt was not
580 significant (Fig. 9g). From the above discussion, it can be concluded that the
581 petrogenesis of the diorites in the NCC was associated with minor fractional
582 crystallization processes. Whole-rock La/Yb versus La and Zr/Sr versus Zr
583 correlations are as expected for a partial melting process (Figs. 9h-i). This implies that
584 the formation of the diorites may be closely related to the partial melting of a basaltic

删除的内容: The diorites from the NCC have similar MgO and low compatible element contents, suggesting that they were not derived directly from a mantle magma source

删除的内容: The magma mixing/mingling with mantle can also be excluded due to their homogeneous initial Nd isotope compositions

删除的内容: SiO₂ contents

删除的内容: intermediate rocks

删除的内容: be the reason for these diorites

删除的内容: The

删除的内容: also

600 protolith.

601 Basement rocks of the lower Taihua Group in the southern margin of the NCC consist 删除的内容: The b
602 of amphibolite (e.g., Diwu et al., 2014, 2018; Wang et al., 2020). Partial melting of
603 amphibolite can also lead to the production of intermediate to acidic magmas (e.g.,
604 Beard and Lofgren, 1991; Rapp and Watson, 1995). The amphibolites of the Taihua
605 Group are characterized by low K content and low K_2O/Na_2O ratios (<0.5, Wang et al.,
606 2019), making it difficult to generate high- K_2O rocks. (Beard and Lofgren, 1991;
607 Roberts and Clemens, 1993). Partial melting of amphibolite typically results in the 删除的内容: The p
608 formation of peraluminous melts (e.g., Beard and Lofgren, 1991; Rapp and Watson,
609 1995), whereas the diorites in the NCC have low Al_2O_3 content with metaluminous
610 character (Fig. 5c; weight average A/NCK values of 0.81). Additionally, the ε_{Nd} values
611 of the Taihua Group amphibolites at $t=1780$ Ma show a wide range from -6.7 to 0.4,
612 different from those of the diorites (Wang et al., 2019). Therefore, it seems unlikely
613 that the diorites formed by the partial melting of Taihua Group amphibolites.

614 Mafic rocks in the Xiong'er Group or the mafic dyke swarms were argued to be the 删除的内容: The m
615 source of the diorites (Cui et al., 2011; Ma et al., 2023b; Peng et al., 2007). The mafic
616 dyke swarms and Xiong'er Group rocks possess a relatively large range of initial Sr
617 and Nd isotopic compositions (Fig. 7d), while the initial Nd isotopic compositions of
618 the diorites are relatively homogeneous (Fig. 7b). Whole-rock initial Nd ratios and the
619 zircon initial Hf isotope ratios of the Xiong'er Group rocks are also enriched (Fig. 7c).
620 The initial Pb isotopic compositions of the mafic dykes and Xiong'er Group rocks are
621 very radiogenic and variable (Fig. 8a, b), which is due to the high U and Th contents
622 of the protolith, indicating the presence of an enriched subcontinental lithospheric
623 mantle source (e.g., Hou et al., 2008; Peng et al., 2004, 2007; Wang et al., 2004, 2010;
624 Zhao et al., 2007). Based on the previous discussion, the geochemical characteristics

638 of the diorites are more compatible with a crustal origin and the isotopic compositions

删除的内容: . These

639 of the diorites indicate that they were not derived from an enriched mantle source,

删除的内容: their sources might not have been derived from the enriched mantle.

640 Additionally, the Xiong'er volcanic rocks have lower Nb/Ta ratios and Nb contents

641 compared to the diorites (Fig. 10a). Nb and Ta share a similar valence state and atomic radii, but they can undergo fractionation during the subduction process.

643 (Jochum et al., 1986; Shannon, 1976). The Xiong'er volcanic rocks, with higher and

644 positively related Ba/Th and Sr/Th ratios (Fig. 10a, b), likely originated from a source influenced by early subduction components, whereas the diorites appear to be less

646 affected by early subduction-related materials. Therefore, it seems likely that the

删除的内容: t

647 were formed by the partial melting of the mafic protolith on top of an

删除的内容: could be

648 enriched subcontinental lithospheric mantle beneath the NCC,

删除的内容: of the lower crust on top of an enriched subcontinental lithospheric mantle beneath the NCC. .

649

650 5.4 Tectonic setting

651 After the Paleoproterozoic collisional amalgamation, the NCC was intruded by
652 diverse magmatic rocks, which have been interpreted as products of continental arc
653 magmatism, post-collisional extension, or continental rift/mantle plume magmatism.

654 The volcanic rocks of the Xiong'er Group along the southern margin of the NCC are

655 dominated by andesites, exhibiting calc-alkaline characteristics, Nb-Ta-Ti anomalie
656 (Jia, 1987, He et al., 2009; Zhao et al., 2009). These signatures together with Nd
657 isotopic evidence for ancient crustal assimilation and multiphase volcanic activities,
658 support a continental arc environment for the formation of the Xiong'er Group (He
659 et al., 2009; Zhao et al., 2009s).

660 The radially distributed mafic dike swarms, accompanied by A-type granite intrusions
661 and rift-related sedimentary sequences, are indicative of a continental rift setting (e.g.,

671 Fan et al., 2024; Xu et al., 2008; Zhao et al., 2002; Zhao et al., 2002, 2007). The
672 Xiong'er Group is dominated by andesite and dacite-rhyolite with minor basaltic
673 andesite, which some researchers interpret as an atypical bimodal suite suggestive of a
674 continental rift setting (Zhao et al., 2002, 2007). Furthermore, the 1.80 to 1.75 Ga old
675 mafic dike swarms can be distributed in a radial or concentric pattern centered on the
676 Xiong'er Rift and extending northward (Peng et al., 2007). They shared geochemical
677 characteristics, such as high TiO₂ and MgO contents, enrichment in LREEs, Ba, and K,
678 and depletion in Nb-Ta are interpreted as evidence for lithospheric extension induced
679 by mantle plume upwelling (e.g., Peng et al., 2007, 2008; Hou et al., 2008).

680 The post-collisional extension model emphasizes that the late Paleoproterozoic
681 magmatism occurred during lithospheric delamination and possibly slab detachment
682 (e.g., Wang et al., 2004, 2008, 2014, 2023a). The mafic dikes are enriched in LILEs
683 and LREEs but depleted in HFSEs, and show negative $\varepsilon_{Nd}(t)$ and $\varepsilon_{Hf}(t)$ values. This
684 suggests derivation from an enriched lithospheric mantle previously metasomatized
685 by subduction fluids (e.g., Hu et al., 2010; Wang et al., 2004, 2008, 2014) These dikes
686 are concentrated in the Trans-North China Orogen and nearby areas, consistent with
687 extensional fractures caused by rising asthenosphere (Wang et al., 2004, 2008, 2014).
688 Their geochemical features, lacking OIB or asthenospheric mantle affinities, do not
689 support a dominant mantle plume origin. (Wang et al., 2014).

690 Calk-alkaline diorites are important intermediate rock that typically forms in island
691 arcs, subduction zones, and continental collision orogenic belts along the convergent
692 plate boundaries. Island arc intermediate rocks, such as boninites and low MgO, high
693 Al₂O₃, and Na₂O/K₂O > 1 andesites are generally characterized by high MgO, Cr, and
694 Ni contents (Hickey et al., 1982; Rapp and Watson, 1995). whereas continental arc
695 intermediate rocks typically show high Al₂O₃ content with a wider range of ⁸⁷Sr/⁸⁶Sr

删除的内容: Diorite

删除的内容: is an

带格式的: 下标

带格式的: 下标

带格式的: 下标

带格式的: 下标

删除的内容: Oceanic island arc intermediate rocks are generally characterized by high MgO, Cr, and Ni contents as boninite and low MgO, high Al₂O₃, and Na₂O/K₂O > 1 andesite

删除的内容: The

705 and $^{143}\text{Nd}/^{144}\text{Nd}$ isotope compositions, reflecting an obvious influence of continental
706 crust more complex and enriched source (Hawkesworth et al., 1979; Peacock et al.,
707 1994). The Paleoproterozoic diorites in the NCC lack the compositional features of
708 arc-related rocks, meanwhile, their trace element distributions differ from those of
709 island arc and continental arc intermediate rocks. For example, the diorites do not
710 show significant enrichment in Sr, Th, and U in the primitive mantle-normalized
711 diagram as arc-related rocks (Fig. 6a). These diorites also exhibit a negative Eu
712 anomaly in the REE diagram, which is different from the arc-related rocks (Fig. 6b).
713 Diorites in collisional orogenic belts have high MgO and K₂O contents and
714 adakite-like characteristics with high Sr/Y and La/Yb ratios (Yang et al., 2015).
715 However, Paleoproterozoic diorites of the NCC do not show the typical arc-related
716 element and isotopic signatures, suggesting formation in a non-subduction
717 environment.
718 Diorites can also form during crustal extension (Asmerom et al., 1990; Liu et al.,
719 2024). The NCC was in a post-collisional extensional environment after the
720 amalgamation (e.g., Zhai, 2010). During this stage magmatism becomes more
721 complex (Bonin, 2004). Zircon is a very stable mineral and its trace elements offer
722 significant potential for distinguishing between different tectonic environments.
723 Zircon samples with La contents less than 1 ppm were selected for discussion to
724 ensure accurate information from zircon trace element contents without interference
725 from the inclusion of other accessory phases (Zou et al., 2019). All zircons from the
726 diorites plot within the continental area in the U/Yb versus Y diagram (Fig. 11a), and
727 most of them fall into a rift-controlled tectonic environment in tectonic discrimination
728 diagrams (Fig. 11b, c; Carly et al., 2014).
729 Furthermore, HFSE elements, such as Zr, Nb, Ta, Hf, and Th, are important in

删除的内容: The
删除的内容: these features of

删除的内容: se

删除的内容: have

删除的内容: The d

删除的内容: in the North China Craton

删除的内容: suggesting a different formation environment from subduction-related magmatism.

删除的内容: Diorites can still form through crustal extension

删除的内容: North China Craton

删除的内容: ,

带格式的: 字体: 小四

删除的内容: where the magmatic genesis became more complex

删除的内容: Zircon is relatively stable and may record more information, therefore, its trace elements offer significant potential for distinguishing between different tectonic environments.

删除的内容: tend to

删除的内容: the zircon tectonic discrimination diagrams

删除的内容: high-field strength elements

757 tectonic discriminators, The distinctive Th content in arc magmas is primarily due to
758 its low solubility in subduction zone fluids and its contribution from sedimentary
759 components (e.g., Bailey and Ragnasdottir, 1994; Pearce and Peate, 1995).

760 Arc-related/orogenic magmas usually have less Nb than those in within-plate settings
761 (e.g., Pearce and Peate, 1995; Sun and McDonough, 1989). Nb in zircon is thought to
762 be incorporated through xenotime-type substitution (Schulz et al., 2006) and is
763 suggested to reflect the magma composition with minimal influence from magmatic
764 fractionation (Hoskin et al., 2000; Schulz et al., 2006). In the Nb/Hf versus Th/U and
765 Hf/Th versus Th/Nb diagrams, zircons from the Fudian and Gushicun diorites plot
766 both within or close to the arc-related/orogenic area (Fig. 11d, e). The Jiuganshan and
767 Muzhijie diorites plot both in the arc-related/orogenic and within-plate/anorogenic
768 areas (Fig. 11d, e). Whole-rock Ta/Yb and Th/Yb ratios of these diorites are uniform
769 (Fig. 11f), all falling within the overlapping area of the ACM (active continental
770 margins) and WPVZ (Within-Plate Volcanic Zone). This may indicate that the

771 post-collisional extension during this period proceeded continuously and
772 progressively into a rift evolution. Nevertheless, the diorites preserve a record of the
773 superimposition of representative components from multiple tectonic settings.

774 After the ~1.85 Ga collisional event, the North China Craton entered a prolonged
775 post-collisional extensional stage. During this stage, magmatism was primarily
776 controlled by crustal thickening and remelting, leading to the widespread formation of
777 various crust-derived granites (e.g., Geng et al., 2006; Zhao et al., 2008, 2018).
778 Subsequent slab breakoff and gravitational collapse of the thickened crust triggered
779 extension in the mid-upper crust and emplacement of felsic magmas (Deng et al.,
780 2016a; Wang et al., 2023a; Xu et al., 2024). At 1.78 Ga, further lithospheric thinning
781 induced upwelling of the asthenosphere, causing further partial melting of previously

删除的内容: discrimination diagrams

删除的内容: The a

删除的内容: and near this area

删除的内容: The w

删除的内容: ese

删除的内容: may ultimately lead to rift evolution continuously and progressively. The diorites preserve a record of the superimposition of representative components from multiple tectonic settings.

删除的内容: The

删除的内容: in the orogenic belts

删除的内容: at the end of the Paleoproterozoic (Deng et al., 2016; Wang et al., 2023b; Xu et al., 2024)

798 subduction-fluid-metasomatized lithospheric mantle (e.g., Peng et al., 2007, 2008;
799 Wang et al., 2010, 2014; Zhao et al., 2002, 2007). Following this event, magmatic
800 activity in the region became dominated by A-type granites and alkaline rocks,
801 marking a transition to an anorogenic intracontinental extensional setting (e.g., Deng
802 et al., 2016b; Wang et al., 2024). The 1.78 Ga crust-derived diorites show transitional
803 features in their tectonic setting, retaining some remnant effects of the orogenic
804 magmatism while gradually evolving toward intraplate magmatism. It reflects the
805 ongoing extension of the North China Craton after its amalgamation.

删除的内容: However, after

删除的内容: 1.78 Ga,

删除的内容: t

806

807 6 Conclusions

808 The Jiguanshan diorite yields a zircon U-Pb age of c. 1.78 Ga. The intrusion displays
809 geochemical features in common with other diorite intrusions within the NCC. The
810 diorite emplaced contemporaneous with the Xiong'er volcanic rocks and the mafic
811 dyke swarms, representing a significant period of magmatism in the NCC.

删除的内容: about

删除的内容: It displays geochemical features in common with other diorite intrusions within the NCC.

删除的内容: intrusion was

812 The late Paleoproterozoic diorites were produced by partial melting of a mafic
813 protolith. The Sr-Nd-Pb-Hf isotopic characteristics indicate that the source was not the
814 same as that for the Xiong'er volcanic rocks or mafic dyke swarms. Instead, they are
815 more likely derived from the lower crust of the NCC.

删除的内容: primarily resulted from the partial melting of the mafic protolith.

816 The formation of Paleoproterozoic diorites in the NCC is not related to arc
817 magmatism. Instead, it is associated with a rift setting. The formation of diorite
818 records the transition of crustal origin rocks from orogenic-related magmatism to
819 intraplate magmatism during the post-collision extensional stage. It reflects the
820 ongoing extension of the North China Craton after its amalgamation.

删除的内容: North China Craton is unlikely to be arc-related.

835 **Acknowledgements**

836 This study was financially supported by the Strategic Priority Research Program of
837 the Chinese Academy of Sciences (grant Nos. XDA0430203) and the National
838 Natural Science Foundation of China (grant Nos. 42202069 and 41872049). Zhiyi
839 Wang was financially supported by China Scholarship Council (202306340065). We
840 thank P. Xiao and Z.-H. Hou for assistance with the analysis.

841 |

删除的内容: .

843 **References**

844 Asmerom, Y., Snow, J. K., Holm, D. K., Jacobsen, S. B., Wernicke, B. P., and Lux, D. R.: Rapid uplift
845 and crustal growth in extensional environments: An isotopic study from the Death Valley region,
846 California. *Geology*, 18, 223–226.
847 [https://doi.org/10.1130/0091-7613\(1990\)018<0223:RUACGI>2.3.CO;2](https://doi.org/10.1130/0091-7613(1990)018<0223:RUACGI>2.3.CO;2), 1990.

848 Bailey, E.H., and Ragnarsdottir, K.V.: Uranium and thorium solubilities in subduction zone fluids.
849 *Earth Planet. Sci. Lett.*, 124, 119–129. [https://doi.org/10.1016/0012-821X\(94\)00071-9](https://doi.org/10.1016/0012-821X(94)00071-9), 1994.

850 Beard, J.S., and Lofgren, G.E.: Dehydration melting and water-saturated melting of basaltic and
851 andesitic greenstones and amphibolites at 1, 3, and 6.9 kb. *J. Petrol.* 32, 365–401.
852 <https://doi.org/10.1093/petrology/32.2.365>, 1991.

853 BGMRH (Bureau of Geology and Mineral Resources of Henan Province): Geological map of the
854 Henan Province. Sheet I-49-(23) (Lushan) scale 1:200,000 (in Chinese), 1994.

855 Bonin, B.: Do coeval mafic and felsic magmas in post-collisional to within-plate regimes necessarily
856 imply two contrasting, mantle and crustal sources? A review. *Lithos*, 78, 1–24.
857 <https://doi.org/10.1016/j.lithos.2004.04.042>, 2004.

858 Carley, T.L., Miller, C.F., Wooden, J.L., Padilla, A.J., Schmitt, A.K., Economos, R.C., Bindeman, I.N.,
859 and Jordan, B.T.: Iceland is not a magmatic analog for the Hadean: evidence from the zircon record.
860 *Earth Planet. Sci. Lett.*, 405, 85–97. <https://doi.org/10.1016/j.epsl.2014.08.015>, 2014.

861 Castillo, P., Janney, P., and Solidum, R.: Petrology and geochemistry of Camiguin Island, southern
862 Philippines: insights to the source of adakites and other lavas in a complex arc setting. *Contrib.
863 Mineral. Petrol.*, 134, 33–51. <https://doi.org/10.1007/s004100050467>, 1999.

864 Chen, F., Hegner, E., and Todt, W.: Zircon ages, Nd isotopic and chemical compositions of
865 orthogneisses from the Black Forest, Germany - evidence for a Cambrian magmatic arc. *Int. J. Earth
866 Sci.*, 88, 791–802. <https://doi.org/10.1007/s005310050306>, 2000.

867 Chen, F., Li, X. H., Wang, X. L., Li, Q. L., and Siebel, W.: Zircon age and Nd-Hf isotopic composition
868 of the Yunnan Tethyan belt, southwestern China. *Int. J. Earth Sci.*, 96, 1179–1194.
869 <https://doi.org/10.1007/s00531-006-0146-y>, 2007.

870 Chen, L., Zheng, Y.F., Xu, Z., and Zhao, Z.F.: Generation of andesite through partial melting of basaltic
871 metasomatites in the mantle wedge: Insight from quantitative study of Andean andesites. *Geosci.
872 Front.*, 12, 101124. <https://doi.org/10.1016/j.gsf.2020.12.005>, 2021.

873 Cui, M.L., Zhang, B.L., Peng, P., Zhang, L.C., Shen, X.L., Guo, Z.H., and Huang, X.F.:
874 Zircon/baddeleyite U-Pb dating for the Paleoproterozoic intermediate-acid intrusive rocks in
875 Xiaoshan Mountains, west of Henan Province and their constraints on the age of the Xiong'er
876 Volcanic Province. *Acta Petrol. Sin. (in Chinese with English abstract)*, 26, 1541–1549, 2010.

877 Cui, M.L., Zhang, B.L., and Zhang, L.C.: U-Pb dating of baddeleyite and zircon from the Shizhaigou
878 diorite in the southern margin of North China Craton: Constraints on the timing and tectonic setting
879 of the Paleoproterozoic Xiong'er group. *Gondwana Res.*, 20, 184-193.
880 <https://doi.org/10.1016/j.gr.2011.01.010>, 2011.

881 Defant, M., and Drummond, M.: Derivation of some modern arc magmas by melting of young
882 subducted lithosphere. *Nature*, 347, 662-665. <https://doi.org/10.1038/347662a0>, 1990.

883 Deng, X. Q., Peng, T. P., and Zhao, T. P.: Geochronology and Geochemistry of the Late
884 Paleoproterozoic Aluminous A-Type Granite in the Xiaoqinling Area along the Southern Margin of
885 the North China Craton: Petrogenesis and Tectonic Implications. *Precambrian Res.*, 285: 127-146.
886 <https://doi.org/10.1016/j.precamres.2016.09.013>, 2016a

887 [Deng, X.Q., Zhao, T.P., and Peng, T.P.: Age and geochemistry of the early Mesoproterozoic A-type
888 granites in the southern margin of the North China Craton: Constraints on their petrogenesis and
889 tectonic implications, Precambrian Research, 283, 68-88,
890 https://doi.org/10.1016/j.precamres.2016.07.018, 2016b.](#)

891 Diwu, C.R., Liu, X., and Sun, Y.: The composition and evolution of the Taihua Complex in the southern
892 North China Craton. *Acta Petrol. Sin.* (in Chinese with English abstract), 34, 999-1018, 2018.

893 Diwu, C.R., Sun, Y., Zhao, Y., and Lai, S.C.: Early Paleoproterozoic (2.45-2.20 Ga) magmatic activity
894 during the period of global magmatic shutdown: Implications for the crustal evolution of the
895 southern North China Craton. *Precambrian Res.*, 255, 627-640.
896 <https://doi.org/10.1016/j.precamres.2014.08.001>, 2014.

897 [Fan, Y. H., Zhu, X. Y., Duan, Q. S., Ma, J. F., Jia, C. Y., Liu, S. Q., and Zhao, T. P.: Discovery of 1.79
898 Ga dacite porphyry in the Taiyueshan Mts: Constraints on the genesis of the southern rift system in
899 the North China Craton, Acta Petrologica Sinica \(in Chinese with English abstract\), 40\(4\), 1327-
900 1342, https://doi.org/10.18654/1000-0569/2024.04.17, 2024.](#)

901 Gao, J.F., Zhou, M.F., Robinson, P.T., Wang, C.Y., Zhao, J.H., and Malpas, J.: Magma mixing recorded
902 by Sr isotopes of plagioclase from dacites of the Quaternary Tengchong volcanic field, SE Tibetan
903 Plateau. *J. Asian Earth Sci.*, 98, 1-17. <https://doi.org/10.1016/j.jseas.2014.10.036>, 2015.

904 Geng, Y.S., Du, L.L., and Ren, L.D.: Growth and reworking of the early Precambrian continental crust
905 in the North China Craton: Constraints from zircon Hf isotopes. *Gondwana Res.*, 21, 517-529.
906 <https://doi.org/10.1016/j.gr.2011.07.006>, 2012.

907 [Geng, Y. S., Yang, C. H., and Wan, Y. S.: Paleoproterozoic granitic magmatism in Lüliang area, North
908 China Craton: constraint from isotopic geochronology, Acta Petrologica Sinica \(in Chinese with
909 English abstract\), 22, 305-314, 2006.](#)

910 Gorton, M.P., and Schandl, E.S.: From continents to island arcs: A geochemical index of tectonic
911 setting for arc-related and within-plate felsic to intermediate volcanic rocks. *Can. Mineral.*, 38,
912 1065-1073. <https://doi.org/10.2113/gscanmin.38.5.1065>, 2000.

913 Grimes, C.B., John, B.E., Kelemen, P.B., Mazdab, F., Wooden, J.L., Cheadle, M.J., Hanghøj, K., and
914 Schwartz, J.J.: Trace element chemistry of zircons from oceanic crust: a method for distinguishing
915 detrital zircon provenance. *Geology*, 35, 643-646. <https://doi.org/10.1130/G23603A.1>, 2007.

916 Hawkesworth, C.J., Norry, M.J., Roddick, J.C., Baker, P.E., Francis, P.W., and Thorpe, R.S.:
917 $^{143}\text{Nd}/^{144}\text{Nd}$, $^{87}\text{Sr}/^{86}\text{Sr}$, and incompatible element variations in calc-alkaline andesites and
918 plateau lavas from South America. *Earth Planet. Sci. Lett.*, 42, 45-57.
919 [https://doi.org/10.1016/0012-821X\(79\)90189-4](https://doi.org/10.1016/0012-821X(79)90189-4), 1979.

920 Hawkesworth, C.J., and Kemp, A.I.S.: Using hafnium and oxygen isotopes in zircons to unravel the
921 record of crustal evolution. *Chem. Geol.*, 226, 144-162.
922 <https://doi.org/10.1016/j.chemgeo.2005.09.018>, 2006.

923 He, J., Qi, Y., Fan, X., and Chen, F.: Petrogenesis of the Taishanmiao A-type granite in the eastern
924 Qinling orogenic belt: Implications for tectonic transition and mineralization in the Late Cretaceous.
925 *J. Geol.*, 129, 97-114. <https://doi.org/10.1086/713726>, 2021.

926 He, Y.H., Zhao, G.C., Sun, M., and Wilde, S.A.: Geochemistry, isotope systematics and petrogenesis of
927 the volcanic rocks in the Zhongtiao Mountain: An alternative interpretation for the evolution of the
928 southern margin of the North China Craton. *Lithos*, 102, 158-178.
929 <https://doi.org/10.1016/j.lithos.2007.09.004>, 2008.

930 He, Y.H., Zhao, G.C., Sun, M., and Xia, X.: SHRIMP and LA-ICP-MS zircon geochronology of the
931 Xiong'er volcanic rocks: Implications for the Paleo-Mesoproterozoic evolution of the southern
932 margin of the North China Craton. *Precambrian Res.*, 168, 213-222.
933 <https://doi.org/10.1016/j.precamres.2008.09.011>, 2009.

934 He, Y.H., Zhao, G.C., Sun, M., and Han, Y.G.: Petrogenesis and tectonic setting of volcanic rocks in the
935 Xiaoshan and Waifangshan areas along the southern margin of the North China Craton: Constraints
936 from bulk-rock geochemistry and Sr-Nd isotopic composition. *Lithos*, 114, 186-199.
937 <https://doi.org/10.1016/j.lithos.2009.08.008>, 2010.

938 Hickey, R.L., and Frey, F.A.: Geochemical characteristics of boninite series volcanics: implications for
939 their source. *Geochim. Cosmochim. Acta*, 46(11), 2099-2115.
940 [https://doi.org/10.1016/0016-7037\(82\)90188-0](https://doi.org/10.1016/0016-7037(82)90188-0), 1982.

941 Hou, G.T., Li, J.H., Yang, M.H., Yao, W.H., Wang, C.C., and Wang, Y.X.: Geochemical constraints on
942 the tectonic environment of the Late Paleoproterozoic mafic dyke swarms in the North China
943 Craton. *Gondwana Res.*, 13, 103-116. <https://doi.org/10.1016/j.gr.2007.06.005>, 2008.

944 Hoskin, P.W.O., Kinny, P.D., Wyborn, D., and Chappell, B.W.: Identifying accessory mineral saturation
945 during differentiation in granitoid magmas: an integrated approach. *J. Petrol.*, 41, 1365-1396.
946 <https://doi.org/10.1093/petrology/41.9.1365>, 2000.

947 [Hu, G. H., Hu, J. L., Chen, W., and Zhao, T. P.: Geochemistry and tectonic setting of the 1.78 Ga mafic](#)
948 [dyke swarms in the Mt. Zhongtiao and Mt. Song areas, the southern margin of the North China](#)
949 [Craton, Acta Petrologica Sinica \(in Chinese with English abstract\), 26, 1563-1576, 2010.](#)

950 Hu, G.Y., Zeng, L.S., Gao, L.E., Liu, Q.P., Chen, H., and Guo, Y.S.: Diverse magma sources for the
951 Himalayan leucogranites: Evidence from B-Sr-Nd isotopes. *Lithos*, 314-315, 88-99.
952 <https://doi.org/10.1016/j.lithos.2018.05.022>, 2018.

953 Huang, X.L., Xu, Y.G., and Liu, D.Y.: Geochronology, petrology and geochemistry of the granulite
954 xenoliths from Nushan, east China: implication for a heterogeneous lower crust beneath the
955 Sino-Korean Craton. *Geochim. Cosmochim. Acta*, 68, 127-149.
956 [https://doi.org/10.1016/S0016-7037\(03\)00416-2](https://doi.org/10.1016/S0016-7037(03)00416-2), 2004.

957 Jackson, M.D., Cheadle, M.J., and Atherton, M.P.: Quantitative modeling of granitic melt generation
958 and segregation in the continental crust. *J. Geophys. Res. Solid Earth*, 108, 2332.
959 <https://doi.org/10.1029/2001JB001050>, 2003.

960 [Jia, C.Z., Petro-geochemistry of volcanic rocks in the Xiong'er Group: implications for tectonic setting.](#)
961 [Henan Geol. 2:39-43 \(in Chinese with English abstract\), 1985.](#)

962 Jochum, K.P., Seufert, H.M., Spettel, B., and Palme, H.: The solar-system abundances of Nb, Ta, and Y,
963 and the relative abundances of refractory lithophile elements in differentiated planetary bodies.
964 *Geochim. Cosmochim. Acta*, 50, 1173-1183. [https://doi.org/10.1016/0016-7037\(86\)90400-X](https://doi.org/10.1016/0016-7037(86)90400-X), 1986.

965 Kelemen, P.B.: Genesis of high Mg[#] andesites and the continental crust. *Contrib. Mineral. Petrol.*, 120,
966 1-19. <https://doi.org/10.1007/BF00311004>, 1995.

967 [Kröner, A., Compston, W., Zhang, G.-W., Guo, A.-L., and Todt, W.: Age and tectonic setting of Late](#)
968 [Archean greenstone-gneiss terrain in Henan Province, China, as revealed by single-grain zircon](#)
969 [dating.](#) *Geology*, 16, 211-215,
970 [https://doi.org/10.1130/0091-7613\(1988\)016<0211:AATSOL>2.3.CO;2](https://doi.org/10.1130/0091-7613(1988)016<0211:AATSOL>2.3.CO;2), 1988.

971 Le Bas, M.J., Le Maitre, R.W., Streckeisen, A., and Zanettin, B.: A Chemical Classification of
972 Volcanic-Rocks Based on the Total Alkali Silica Diagram. *J. Petrol.*, 27, 745-750.
973 <https://doi.org/10.1093/petrology/27.3.745>, 1986.

974 [Li, X. P., Yang, Z. Y., Zhao, G. C., Grapes, R., and Guo, J. H.: Geochronology of khondalite-series](#)
975 [rocks of the Jining Complex: Confirmation of depositional age and tectonometamorphic evolution](#)
976 [of the North China craton, Int. Geol. Rev.](#), 53, 1194-1211, doi:10.1080/00206810903548984, 2011.

977 Liu, A.L., Hai, L.F., Liu, J.K., Zhang X.J., Li H.F., Zhao F.S., Zhao G.L., and Bai J.H.: Geochronology,
978 Geochemistry, and Sr-Nd-Hf Isotopes of the Diorite Porphyrites from the Weining Beishan Area,
979 Ningxia Hui Autonomous Region: Constraints on Their Source and Tectonic Implications. *J. Earth*
980 *Sci.* 35, 462-475. <https://doi.org/10.1007/s12583-021-1491-2>, 2024.

981 Liu, D.Y., Nutman, A.P., Compston, W., Wu, J.S., and Shen, Q.H.: Remnants of ≥ 3800 Ma crust in the
982 Chinese part of the Sino-Korean Craton. *Geology*, 20, 339-342.
983 [https://doi.org/10.1130/0091-7613\(1992\)020<0339:ROMCIT>2.3.CO;2](https://doi.org/10.1130/0091-7613(1992)020<0339:ROMCIT>2.3.CO;2), 1992.

984 Liu, Y.S., Hu, Z.C., Zong, K.Q., Gao, C.G., Gao, S., Xu, J.A., and Chen, H.H.: Reappraisal and
985 refinement of zircon U-Pb isotope and trace element analyses by LA-ICP-MS. *Chin. Sci. Bull.* (in
986 Chinese with English abstract), 1535-1546, 2010.

987 [Lu, S.N., Zhao, G.C., Wang, H.C., and Hao, G.J.: Precambrian metamorphic basement and sedimentary](#)
988 [cover of the North China Craton: A review. *Precambrian Res.*, 160, 77-93, 2008.](#)

989 Ma, J.F., Qu, C.H., Zhou, Y.Y., and Zhao, T.P.: The genesis of *ca.* 1.78 Ga granitoids in the Xiong'er
990 large igneous province: Implications for continental crust generation. *Geol. Soc. Am. Bull.*, 135,
991 3213-3227. <https://doi.org/10.1130/B36694.1>, 2023a.

992 Ma, J.F., Wang, X.L., Yang, A.Y., and Zhao, T.P.: Tracking crystal-melt segregation and accumulation
993 in the intermediate magma reservoir. *Geophys. Res. Lett.*, 50, e2022GL102540.
994 <https://doi.org/10.1029/2022GL102540>, 2023b.

995 Maniar, P.D., and Piccoli, P.M.: Tectonic discrimination of granitoids. *Geol. Soc. Am. Bull.*, 101,
996 635-643. [https://doi.org/10.1130/0016-7606\(1989\)101<0635:TDOG>2.3.CO;2](https://doi.org/10.1130/0016-7606(1989)101<0635:TDOG>2.3.CO;2), 1989.

997 Pan, Z.J., Zhang, Q., Chen, G., Jiao, S.T., Du, X.L., Miao, X.Q., Wang, J.R., and An, Y.: Relation
998 between Mesozoic magmatism and plate subduction in eastern China: Comparison among
999 Zhejiang-Fujian, Japan arc and Andes arc. *Acta Petrol. Sin.* (in Chinese with English abstract), 33,
1000 1507-1523, 2017.

1001 Peacock, S.M., Rushmer, T., and Thompson, A.B.: Partial melting of subducting oceanic crust. *Earth*
1002 *Planet. Sci. Lett.*, 121, 227-244. [https://doi.org/10.1016/0012-821X\(94\)90042-6](https://doi.org/10.1016/0012-821X(94)90042-6), 1994.

1003 Pearce, J.A.: Role of the sub-continental lithosphere in magma genesis at active continental margins.
1004 In: Hawkesworth, C.J., Norry, M.J. (Eds.): *Continental Basalts and Mantle Xenoliths*. Shiva
1005 Publishing Ltd., Nantwich, 230-249. ISBN: 978-0906812341, 1983.

1006 Pearce, J.A., and Peate, D.W.: Tectonic implications of the composition of volcanic arc magmas. *Annu.*
1007 *Rev. Earth Planet. Sci.*, 23, 251-285. <https://doi.org/10.1146/annurev.ea.23.050195.001343>, 1995.

1008 Peccerillo, A., and Taylor, S.R.: Geochemistry of Eocene calc-alkaline volcanic rocks from the
1009 Kastamonu area, northern Turkey. *Contrib. Mineral. Petrol.*, 58, 130-143.
1010 <https://doi.org/10.1007/BF00384745>, 1976.

1011 Peng, P., Zhai, M.G., Zhang, H.F., Zhao, T.P., and Ni, Z.Y.: Geochemistry and geological significance
1012 of the 1.8 Ga mafic dyke swarms in the North China Craton: an example from the juncture of
1013 Shanxi, Hebei and Inner Mongolia. *Acta Petrol. Sin.* (in Chinese with English abstract), 20,
1014 439-456, 2004.

1015 Peng, P., Zhai, M.G., Guo, J.H., Kusky, T., and Zhao, T.P.: Nature of mantle source contributions and
1016 crystal differentiation in the petrogenesis of the 1.78 Ga mafic dykes in the central North China
1017 craton. *Gondwana Res.*, 12, 29-46. <https://doi.org/10.1016/j.gr.2006.10.022>, 2007.

1018 Peng, P., Zhai, M.G., Ernst, R.E., Guo, J.H., Liu, F., and Hu, B.: A 1.78 Ga large igneous province in
1019 the North China craton: The Xiong'er Volcanic Province and the North China dyke swarm. *Lithos*,
1020 101, 260-280. <https://doi.org/10.1016/j.lithos.2007.07.006>, 2008.

1021 Petford, N., and Atherton, M.: Na-rich partial melts from newly underplated basaltic crust: the
1022 Cordillera Blanca Batholith, Peru. *J. Petrol.*, 37, 1491-1521.
1023 <https://doi.org/10.1093/petrology/37.6.1491>, 1996.

1024 Rapp, R.P., and Watson, E.B.: Dehydration melting of metabasalt at 8–32 kbar: Implications for
1025 continental growth and crust-mantle recycling. *J. Petrol.*, 36, 891-931.
1026 <https://doi.org/10.1093/petrology/36.4.891>, 1995.

1027 Reubi, O., and Blundy, J.: A dearth of intermediate melts at subduction zone volcanoes and the
1028 petrogenesis of arc andesites. *Nature*, 461, 1269-1273. <https://doi.org/10.1038/nature08510>, 2009.

1029 Roberts, M.P., and Clemens, J.D.: Origin of high-potassium, calc-alkaline, I-type granitoids. *Geology*,
1030 21, 825–828. [https://doi.org/10.1130/0091-7613\(1993\)021<0825:OOHPTA>2.3.CO;2](https://doi.org/10.1130/0091-7613(1993)021<0825:OOHPTA>2.3.CO;2), 1993.

1031 Schulz, B., Klemd, R., and Brätz, H.: Host rock compositional controls on zircon trace element
1032 signatures in metabasites from the Austroalpine basement. *Geochim. Cosmochim. Acta*, 70, 697–
1033 710. <https://doi.org/10.1016/j.gca.2005.10.001>, 2006.

1034 Shannon, R.D.: Revised effective ionic-radii and systematic studies of interatomic distances in halides
1035 and chalcogenides. *Acta Crystallogr. A*, 32, 751-767. <https://doi.org/10.1107/S0567739476001551>,
1036 1976.

1037 Shen, F.N.: The discovery of unconformity within the Taihua Group and definition of its stratigraphic
1038 sequence in the Lushan area, Henan. *Reg. Geol. China* (in Chinese with English abstract), 2,
1039 135-140. doi: 10.12097/gbc.ZQYD402.005, 1994.

1040 Siebel, W., Reitter, E., Wenzel, T., and Blaha U.: Sr isotope systematics of K-feldspars in plutonic rocks
1041 revealed by the Rb–Sr microdrilling technique. *Chem. Geol.*, 222, 183–199.
1042 <https://doi.org/10.1016/j.chemgeo.2005.06.012>, 2005.

1043 Stern, C., and Kilian, R.: Role of the subducted slab, mantle wedge and continental crust in the
1044 generation of adakites from the Andean Austral Volcanic Zone. *Contrib. Mineral. Petrol.*, 123,
1045 263-281. <https://doi.org/10.1007/s004100050155>, 1996.

1046 Streck, M.J., Leeman, W.P., and Chesley, J.: High-magnesian andesite from Mount Shasta: A product of
1047 magma mixing and contamination, not a primitive mantle melt. *Geology*, 35, 351-354.
1048 <https://doi.org/10.1130/G23286A.1>, 2007.

1049 Sun, Q.Y., Zhou, Y.Y., Wang, W., Li, C.D., and Zhao, T.P.: Formation and evolution of the
1050 Paleoproterozoic meta-mafic and associated supracrustal rocks from the Lushan Taihua Complex,
1051 southern North China Craton: Insights from zircon U-Pb geochronology and whole-rock
1052 geochemistry. *Precambrian Res.*, 303, 428-444. <https://doi.org/10.1016/j.precamres.2017.05.018>,
1053 2017.

删除的内容: .

1055 Sun, S.S., and McDonough, W.F.: Chemical and isotopic systematics of oceanic basalts: implications
1056 for mantle composition and processes. *Geol. Soc. London, Spec. Publ.*, 42, 313-345.
1057 <https://doi.org/10.1144/GSL.SP.1989.042.01.19>, 1989.

1058 Vermeesch, P.: IsoplotR: A free and open toolbox for geochronology. *Geoscience Frontiers*, 9,
1059 1479-1493. <https://doi.org/10.1016/j.gsf.2018.04.001>, 2018.

1060 Wan, Y.S., Wlide, S., Liu, D.Y., Yang, C.X., Song, B., and Yin, X.Y.: Further evidence for ~1.85 Ga
1061 metamorphism in the Central Zone of the North China Craton: SHRIMP U-Pb dating of zircon
1062 from metamorphic rocks in the Lushan area, Henan Province. *Gondwana Res.*, 9, 189-197,
1063 <https://doi.org/10.1016/j.gr.2005.06.010>, 2006

1064 Wang, C.M., Lu, Y.J., He, X.Y., Wang, Q.H., and Zhang, J.: The Paleoproterozoic diorite dykes in the
1065 southern margin of the North China Craton: Insight into rift-related magmatism. *Precambrian Res.*,
1066 277, 26-46. <https://doi.org/10.1016/j.precamres.2016.02.009>, 2016.

1067 Wang, J.L., Zhang, H.F., Zhang, J., Santosh, M., and Bao, Z. A.: Highly heterogeneous Pb isotope
1068 composition in the Archean continental lower crust: Insights from the high-grade metamorphic suite
1069 of the Taihua Group, Southern North China Craton. *Precambrian Res.*, 350, 105927.
1070 <https://doi.org/10.1016/j.precamres.2020.105927>, 2020.

1071 Wang, M.X., Wang Z.Y., Zhao J.X., Qi Z.Q., He J., and Chen F.K.: Petrogenesis and Geologic
1072 Implication of the Late Paleoproterozoic A-type Xiaohe Pluton along the Southern Margin of the
1073 North China Craton. *Geol. J. China Univ. (in Chinese with English abstract)*, 29(6): 809-830, 2023a.

1074 Wang, X., Huang X., and Yang F.: Revisiting the Lushan-Taihua Complex: New perspectives on the
1075 Late Mesoarchean-Early Neoarchean crustal evolution of the southern North China Craton:
1076 Precambrian Res., 325, 132-149. <https://doi.org/10.1016/j.precamres.2019.02.020>, 2019.

1077 Wang, X.W., Zhu, M., Luo, X., Ren, and X., Cui.: Approximately 1.78 Ga mafic dykes in the Lüliang
1078 Complex, North China Craton: Zircon ages and Lu-Hf isotopes, geochemistry, and implications.
1079 *Geochem. Geophys. Geosyst.*, 15, 3123-3144. doi:10.1002/2014GC005378, 2014.

1080 Wang, X.L., Jiang, S.Y., and Dai, B.Z.: Melting of enriched Archean subcontinental lithospheric
1081 mantle: Evidence from the ca. 1760 Ma volcanic rocks of the Xiong'er Group, southern margin of
1082 the North China Craton. *Precambrian Res.*, 182, 204-216.
1083 <https://doi.org/10.1016/j.precamres.2010.08.007>, 2010.

1084 Wang, Y.J., Fan, W.M., Zhang, Y., Guo, F., Zhang, H., and Peng, T.: Geochemical, $40\text{Ar}/39\text{Ar}$
1085 geochronological and Sr-Nd isotopic constraints on the origin of Paleoproterozoic mafic dikes from
1086 the southern Taihang Mountains and implications for the ca. 1800 Ma event of the North China
1087 Craton. *Precambrian Res.*, 135, 55-77. <https://doi.org/10.1016/j.precamres.2004.07.005>, 2004.

1088 Wang, Y., Zhao, G., Cawood, P. A., Fan, W., Peng, T., and Sun, L.: Geochemistry of Paleoproterozoic
1089 (~1770 Ma) mafic dikes from the Trans-North China Orogen and tectonic implications. *J. Asian*
1090 *Earth Sci.* 33(1-2), 61-77, <https://doi.org/10.1016/j.jseas.2007.10.018>, 2008.

删除的内容: b

删除的内容: .

删除的内容: .

删除的内容: .

删除的内容: .

删除的内容: .

1097 Wang, Z.Y., Zhao, J.X., Qi, Z.Q., Huo, D.Y., Siebel, W., He, J., Li, S.Q., and Chen, F.C.: Two stages of
1098 late Paleoproterozoic A-type granites at the southern North China Craton: Geochemical constraints
1099 and implications for supercontinent breakup, *Precambrian Research*, 411, 107500,
1100 <https://doi.org/10.1016/j.precamres.2024.107500>, 2024.

1101 Wang, Z.Y., Cheng, H., Zhao, J.X., Ye R.S., Li W.Y., He J.F., and Chen F.K.: Sr-Nd-Pb isotopic
1102 composition of the Chinese national standard igneous rock powders measured by thermal ionization
1103 mass spectrometry. *Geol. J. China Univ. (in Chinese with English abstract)*, 29, 679-692, 2023. b

1104 Wolf, M.B., and Wyllie, P.J.: Garnet growth during amphibolite anatexis: Implications of a
1105 garnetiferous restite. *J. Geol.*, 101, 357-373. <https://doi.org/10.1086/648229>, 1993.

1106 Wolf, M., Romer, R.L., and Glodny, J.: Isotope disequilibrium during partial melting of
1107 metasedimentary rocks. *Geochim. Cosmochim. Acta*, 257, 163-183.
1108 <https://doi.org/10.1016/j.gca.2019.05.008>, 2019.

1109 Xu, J.H., Jiang, Y.P., Hu, S.L., Zhang Z.W., Wu C.Q., Zheng C.F., Li X.Y., Jin Z.R., Zhang S.S., and
1110 Zhou Y.T.: Petrogenesis and Tectonic Implications of the Paleoproterozoic A-Type Granites in the
1111 Xiong'ershan Area along the Southern Margin of the North China Craton. *J. Earth Sci.*, 35, 416-
1112 429. <https://doi.org/10.1007/s12583-021-1424-0>, 2024.

1113 Xu, Y.H., Zhao, T.P., Zhang, Y.X., and Chen, W.: Geochemical characteristics and geological
1114 significance of the detrital rocks from the Dagushi Formation of the Paleoproterozoic Xiong'er
1115 Group in the southern North China Craton. *Geological Review*, 54(3), 316-326,
1116 <https://doi.org/10.3321/j.issn:0371-5736.2008.03.004>, 2008.

1117 Xue, L.W., Yuan, Z.L., Zhang, M.S., and Qiang, L.Z.: The Sm-Nd isotope ages of Tai-hua Group in the
1118 Lushan area and their implications. *Geochimica (in Chinese with English abstract)*, 24, 92-97, 1995.

1119 Yang, J.H., Cawood, P.A., Du, Y.S., Huang, H., Huang, H.W., and Tao, P.: Large Igneous Province and
1120 magmatic arc sourced Permian-Triassic volcanogenic sediments in China. *Sedimentary Geol.*
1121 261-262, 120-131. <https://doi.org/10.1016/j.sedgeo.2012.03.018>, 2012.

1122 Yang, Z.M., Lu, Y.J., Hou, Z.Q., and Chang, Z.S.: High-Mg diorite from Qulong in southern Tibet:
1123 implications for the genesis of adakite-like intrusions and associated porphyry Cu deposits in
1124 collisional orogens. *J. Petrol.*, 56, 227-254. <https://doi.org/10.1093/petrology/egu076>, 2015.

1125 Zeng, L.S., Asimow, P.D., and Saleeby, J.B.: Coupling of anatetic reactions and dissolution of
1126 accessory phases and the Sr and Nd isotope systematics of anatetic melts from a metasedimentary
1127 source. *Geochim. Cosmochim. Acta*, 69, 3671-3682. <https://doi.org/10.1016/j.gca.2005.02.035>,
1128 2005.

1129 Zhai, M.G.: Tectonic evolution and metallogenesis of North China Craton. *Mineral Deposits (in*
1130 *Chinese with English abstract)*, 29, 24-36, 2010.

删除的内容: a

删除的内容:

删除的内容:

删除的内容:

1135 | [Zhai M G.: Cratonization and the Ancient North China Continent: A summary and review. Sci China](#)
1136 | [Earth Sci \(in Chinese with English abstract\), 54: 1110–1120, doi: 10.1007/s11430-011-4250-x,](#)
1137 | [2011.](#)

1138 | Zhao, G.C., Cawood, P.A., Wilde, S.A., Min, S., and Lu, L.Z.: Metamorphism of basement rocks in the
1139 | Central Zone of the North China Craton: implications for Paleoproterozoic tectonic evolution.
1140 | *Precambrian Res.*, 103, 55–88. [https://doi.org/10.1016/S0301-9268\(00\)00076-0](https://doi.org/10.1016/S0301-9268(00)00076-0), 2000a.

1141 | Zhao, G.C., He, Y.H., and Sun, M.: Xiong'er volcanic belt at the North China Craton: The Xiong'er
1142 | volcanic belt at the southern margin of the North China Craton: Petrographic and geochemical
1143 | evidence for its outboard position in the Paleo-Mesoproterozoic Columbia Supercontinent.
1144 | *Gondwana Res.*, 16, 170–181. <https://doi.org/10.1016/j.gr.2009.02.004>, 2009.

1145 | Zhao, G.C., Wilde, S.A., Cawood, P.A., and Lu, L.Z.: Petrology and P-T path of the Fuping mafic
1146 | granulites: implications for tectonic evolution of the central zone of the North China Craton. *J.*
1147 | *Metamorphic Geol.*, 18, 375–391. <https://doi.org/10.1046/j.1525-1314.2000.00264.x>, 2000b.

1148 | Zhao, G.C., Wilde, S.A., Cawood, P.A., and Sun, M.: Archean blocks and their boundaries in the North
1149 | China Craton: lithological, geochemical, structural and P-T path constraints and tectonic evolution.
1150 | *Precambrian Res.* 107, 45–73. [https://doi.org/10.1016/S0301-9268\(00\)00154-6](https://doi.org/10.1016/S0301-9268(00)00154-6), 2001.

1151 | [Zhao, G., Wilde, S. A., Sun, M., Li, S., Li, X., and Zhang, J.: SHRIMP U–Pb zircon ages of granitoid](#)
1152 | [rocks in the Lüliang Complex: Implications for the accretion and evolution of the Trans-North](#)
1153 | [China Orogen. Precambrian Research, 160\(3–4\), 213–226,](#)
1154 | <https://doi.org/10.1016/j.precamres.2007.07.004>, 2008.

1155 | [Zhao, G.C., Sun, M., Wilde, S.A., and Li Sanzhong.: Late Archean to Paleoproterozoic evolution of the](#)
1156 | [North China Craton: key issues revisited. Precambrian Res., 136, 177–202](#)
1157 | <https://doi.org/10.1016/j.precamres.2004.10.002>, 2005.

1158 | Zhao, G.C., and Zhai, M.G.: Lithotectonic elements of Precambrian basement in the North China
1159 | Craton: Review and tectonic implications. *Gondwana Res.*, 23, 1207–1240.
1160 | <https://doi.org/10.1016/j.gr.2012.08.016>, 2013.

1161 | [Zhao, J., Zhang, C., Guo, X., and Liu, X.: The late-Paleoproterozoic I- and A-type granites in Lüliang](#)
1162 | [Complex, North China Craton: New evidence on post-collisional extension of Trans-North China](#)
1163 | [Orogen. Precambrian Research, 318, 70–88, <https://doi.org/10.1016/j.precamres.2018.09.007>](#), 2018.

1164 | Zhao, T.P.: The characteristic and genesis of Proterozoic potassic volcanic rock in southern margin of
1165 | the North plate. Doctoral dissertation, Institute of Geology and Geophysics, Chinese Academy of
1166 | Sciences, Beijing, 102p, 2000.

1167 | Zhao, T.P., Xu, Y.H., and Zhai, M.G.: Petrogenesis and tectonic setting of the Paleoproterozoic
1168 | Xiong'er Group in the southern part of the North China Craton: A review. *Geol. J. China Univ.* (in
1169 | Chinese with English abstract), 13, 191–206, 2007.

1170 Zhao, T.P., Zhou, M.F., Zhai, M.G., and Xia, B.: Paleoproterozoic rift-related volcanism of the Xiong'er
1171 Group, North China Craton: Implications for the breakup of Columbia. *Int. Geol. Rev.*, 44, 336-351.
1172 <https://doi.org/10.2747/0020-6814.44.4.336>, 2002

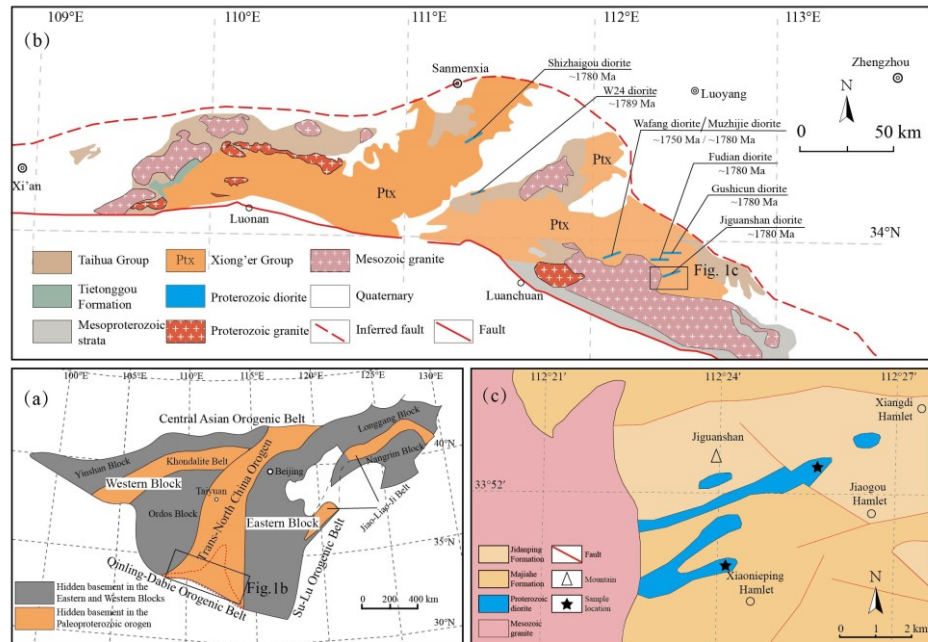
1173 Zhao, T.P., Zhai, M.G., Xia, B., Li, H.M., and Zhang, Y.X.: Zircon U-Pb SHRIMP dating for the
1174 volcanic rocks of the Xiong'er Group: Constraints on the initial formation age of the cover of the
1175 North China Craton. *Chin. Sci. Bull.* (in Chinese with English abstract), 49, 2495-2502, 2004.

1176 Zhang, G.W., Bai, Y.B., Sun, Y., Guo, A.L., Zhou, D.W., and Li, T.H.: Composition and evolution of
1177 the archaean crust in central Henan, China. *Precambrian Res.*, 27, 7-35.
1178 [https://doi.org/10.1016/0301-9268\(85\)90004-X, 1985.](https://doi.org/10.1016/0301-9268(85)90004-X)

1179 Zou, X.Y., Qin, K.Z., Han, X.L., Li, G.M., Evans, N.J., Li, Z.Z., and Yang, W.: Insight into zircon REE
1180 oxy-barometers: A lattice strain model perspective. *Earth Planet. Sci. Lett.*, 506, 87-96.
1181 <https://doi.org/10.1016/j.epsl.2018.10.031>, 2019.

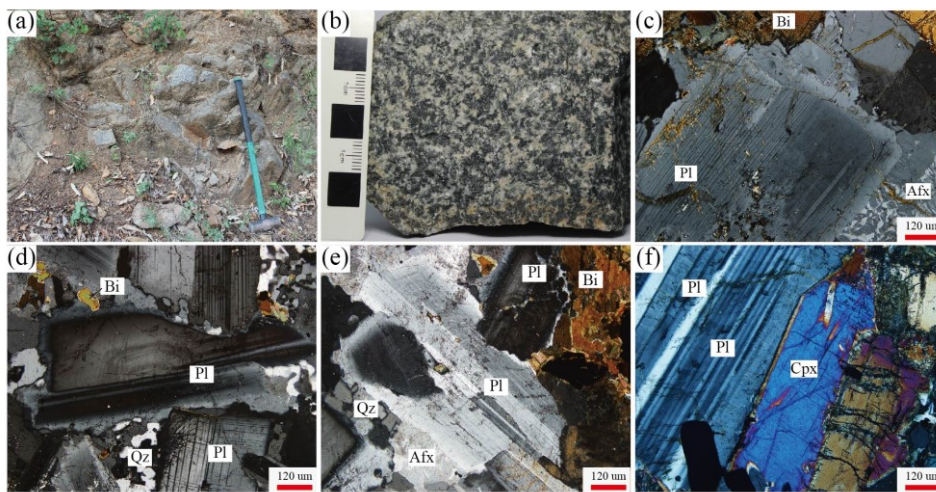
1182

1183 **Figure**



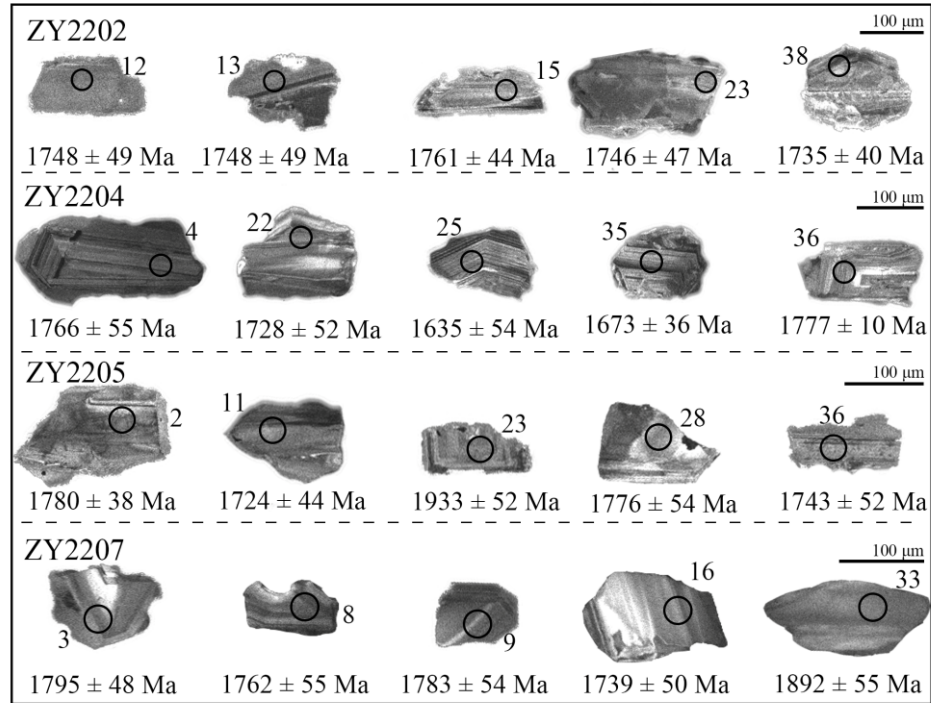
1184

1185 **Figure 1** (a) Tectonic sketch of the North China Craton (after Zhao et al., 2001); (b) Geological map of
1186 the southern margin of the North China Craton (after Diwu et al., 2014; diorites from Cui et al.,
1187 2011; Ma et al 2023a, b; Wang et al., 2016; Zhao et al., 2004); (c) Geological map of the Jiguanshan
1188 diorite (after BGMRH, 1994)



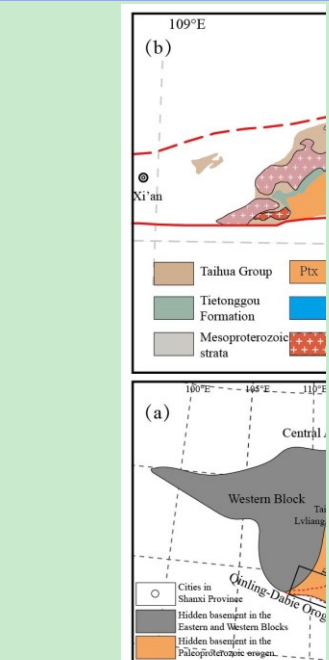
1189

1190 **Figure 2** (a-b) Field photographs and representative hand specimens of the Jiguanshan diorite; (c-f)
1191 Microphotographs under plane-polarized light of the Jiguanshan diorite. Mineral abbreviations:
1192 Afs, alkali feldspar; Bi, biotite; Cpx, Clinopyroxene; Pl, plagioclase; Qz, quartz



1193

1194 **Figure 3** Cathodoluminescence (CL) images of representative zircon grains from the Jiguanshan
1195 diorite



删除的内容:

Figure 1 (a) Tectonic sketch of the North China Craton (after Zhao et al., 2001); (b) Geological map of the southern margin of the North China Craton (after Diwu et al., 2014; diorites from Cui et al., 2011; Ma et al. 2023a, b; Wang et al., 2016; Zhao et al., 2004); (c) Geological map of the Jiguanshan diorite (after BGMRH, 1994).

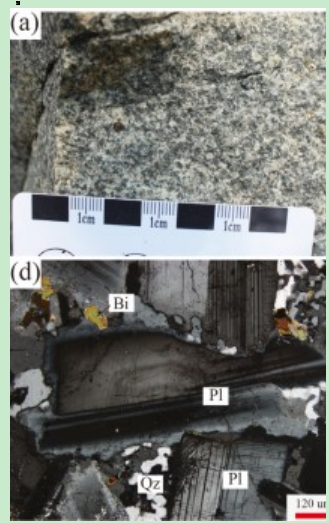
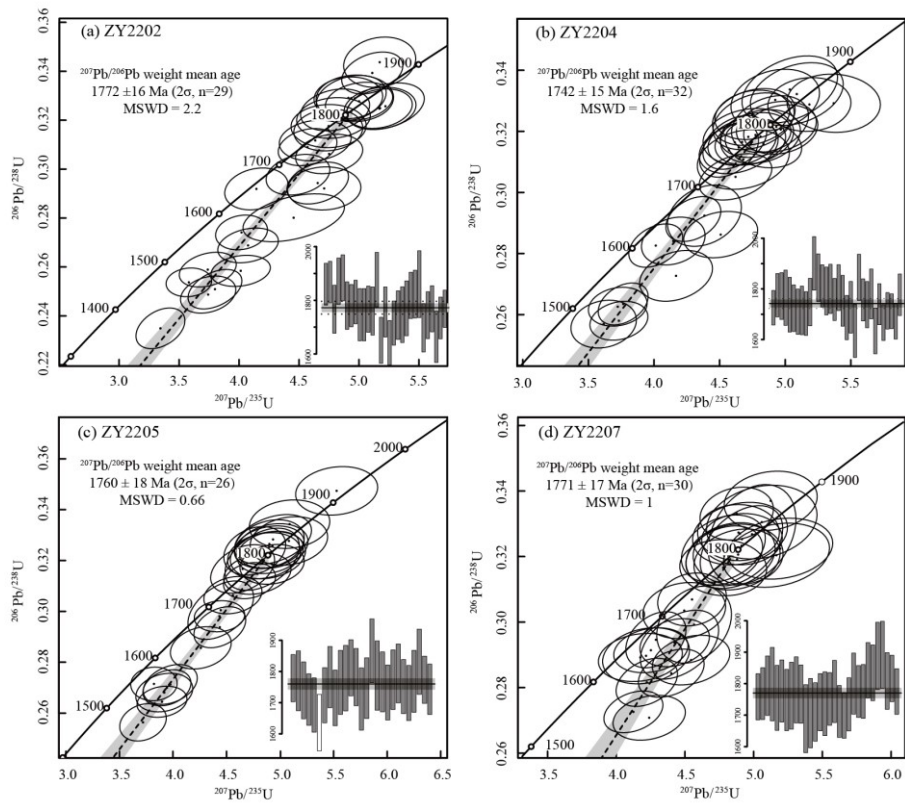
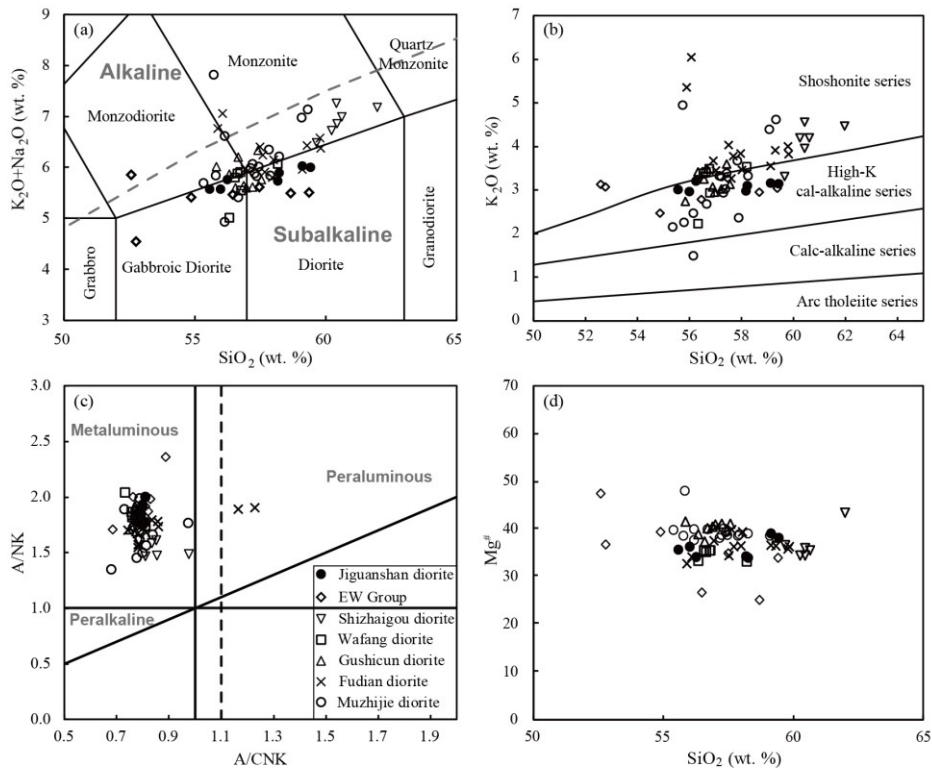


Figure 2 (a-b) Field photographs and representative hand specimens of the Jiguanshan diorite; (c-f) Micrographs under the plane-polarized light of the Jiguanshan diorite. Mineral



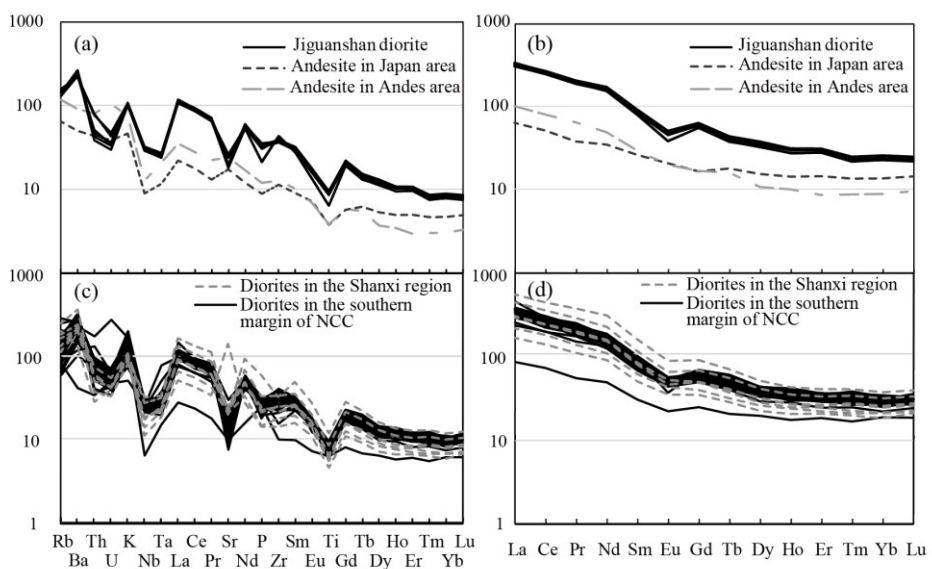
1237

1238 **Figure 4** (a-d) Zircon U-Pb Concordia diagrams of the Jiguanshan diorite



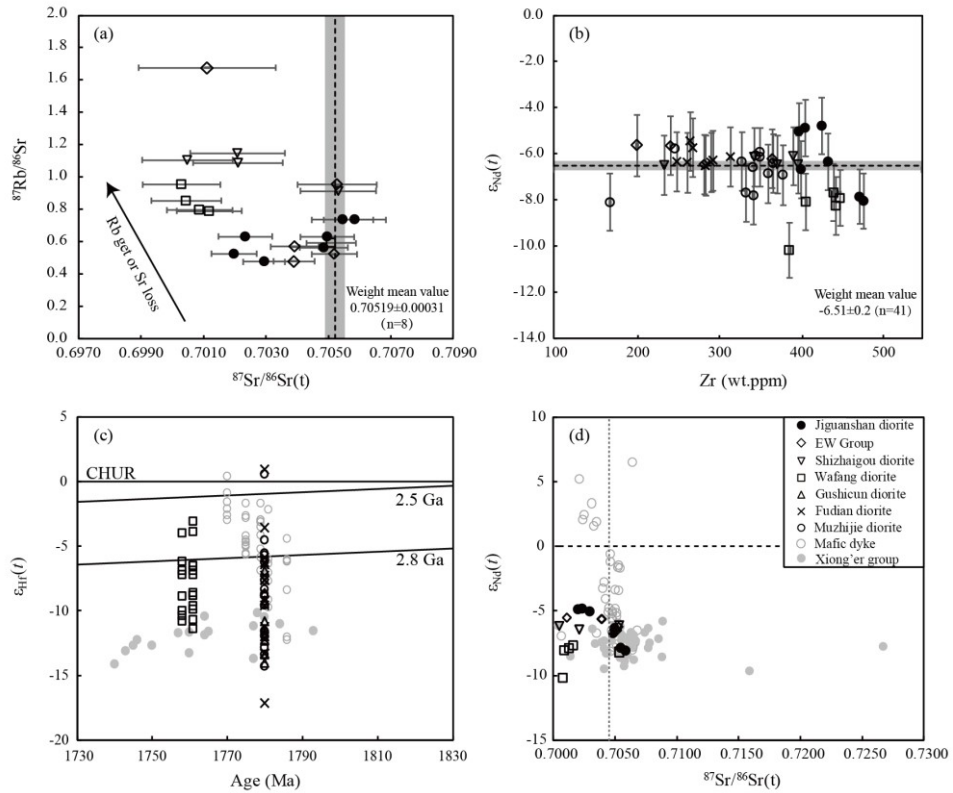
1239

1240 **Figure 5** Plots of major elements for the diorites: (a) TAS diagram (after Le Bas et al., 1986); (b)
1241 K_2O content versus SiO_2 content (after Peccerillo and Taylor, 1976); (c) A/NK versus A/CNK
1242 values (after Maniar and Piccoli, 1989) (d) $Mg^{\#}$ value versus SiO_2 content (wt. %)

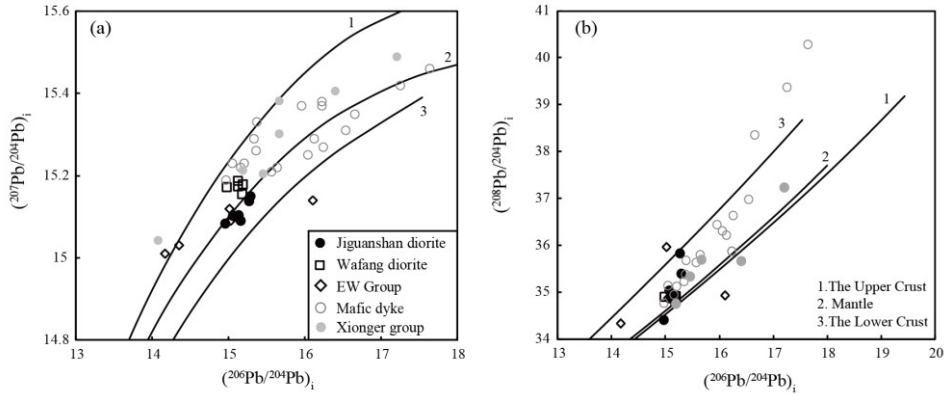


1243

1244 **Figure 6** Primitive-mantle normalized trace element spider diagrams and chondrite-normalized
 1245 REE patterns for the diorites. Normalization values from Sun and McDonough (1989);
 1246 Diorites in Shanxi region from Peng et al. (2007), diorites in the southern margin of the NCC
 1247 from Cui et al. (2011), Ma et al. (2023a, b), Wang et al. (2016), and Zhao et al. (2004). Average
 1248 trace element compositions of intermediate rocks in the Japan and Andes arc are from Pan et
 1249 al. (2017).

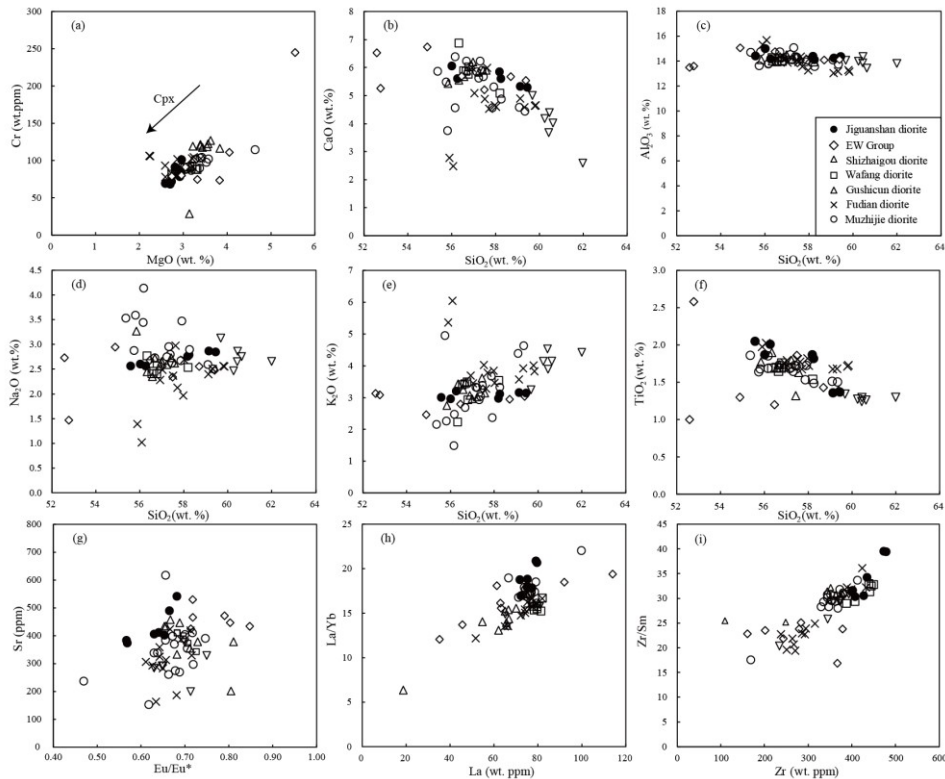


1250
 1251 **Figure 7** (a) $^{87}\text{Rb}/^{86}\text{Sr}$ value versus $^{87}\text{Sr}/^{86}\text{Sr(t)}$ ratio; (b) $\epsilon_{\text{Nd}}(t)$ value versus Zr content (ppm); (c)
 1252 $\epsilon_{\text{Nd}}(t)$ value versus age (Ma); (d) $\epsilon_{\text{Nd}}(t)$ value versus $^{87}\text{Sr}/^{86}\text{Sr(t)}$ ratio. Data source for
 1253 Xiong'er Group (Hf isotope composition from Wang et al., 2010; initial Sr isotope
 1254 composition and initial ϵ_{Nd} value from He et al., 2008, 2010; Peng et al., 2008; Wang et al.,
 1255 2010; Zhao et al., 2002); mafic dyke swarms (initial Sr isotope composition and initial ϵ_{Nd}
 1256 value from Hu et al., 2010; Peng et al., 2007; Wang et al., 2004)



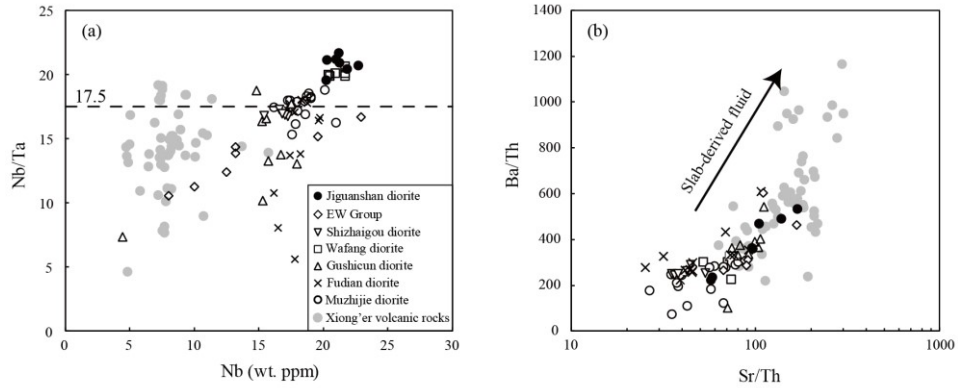
1257

1258 **Figure 8** (a) $(^{207}\text{Pb}/^{204}\text{Pb})_i$ versus $(^{206}\text{Pb}/^{204}\text{Pb})_i$; (b) $(^{208}\text{Pb}/^{204}\text{Pb})_i$ versus $(^{206}\text{Pb}/^{204}\text{Pb})_i$. Data for
1259 Xionger group from Zhao (2000), for mafic dyke swarms from Hu et al. (2010), Peng et al.,
1260 (2007) and for diorites from Peng et al. (2007), Wang et al. (2016)



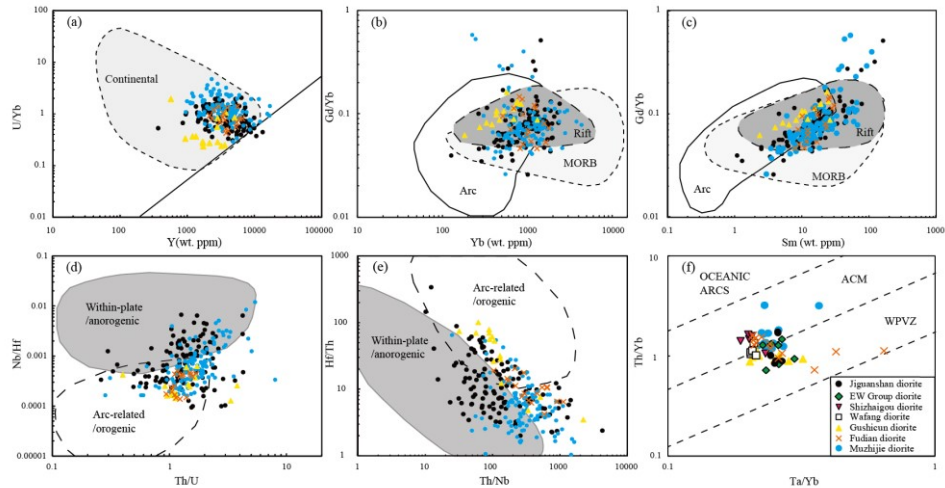
1261

1262 **Figure 9** (a) Cr (wt. ppm) content versus MgO content (wt. %); (b) CaO (wt. %) content versus SiO₂
1263 content (wt. %); (c) Al₂O₃ (wt. %) content versus SiO₂ content (wt. %); (d) Na₂O (wt. %)
1264 content versus SiO₂ content (wt. %); (e) K₂O (wt. %) content versus SiO₂ content (wt. %); (f)
1265 TiO₂ (wt. %) content versus SiO₂ content (wt. %); (g) Eu/Eu* value versus Sr content (ppm);
1266 (h) La/Yb value versus La content (ppm); (i) Zr/Sr value versus Zr content (ppm)



1267

1268 **Figure 10** (a) Nb/Ta versus Nb content (ppm); (b) Ba/Th value versus Sr/Th values; Data for
1269 Xiong'er Group from [He et al. \(2008, 2010\)](#), [Wang et al. \(2010\)](#), [Zhao et al. \(2002\)](#)



1270

1271 **Figure 11** (a) Zircon trace element U/Yb value versus Y (ppm) (after [Grimes et al., 2007](#)); (b)
1272 Zircon trace element Gd/Yb value versus Yb (ppm) (after [Carley et al., 2014](#)); (c) Zircon
1273 trace element Gd/Yb value versus Sm (ppm) (after [Carley et al., 2014](#)); (d) Zircon trace
1274 element Nb/Hf value versus Th/U value (after [Hawkesworth and Kemp, 2006](#)); (e) Zircon
1275 trace element Hf/Tb value versus Th/Nb value (after [Yang et al., 2012](#)); (f) Whole-rock trace
1276 element Th/Yb value versus Ta/Yb value (after [Pearce, 1983](#); [Gorton and Schandl, 2000](#));
1277

1278 **Tables**1279 **Table 1** Major (wt. %) and trace element contents (ppm) of the Jiguanshan diorite

Sample No.	ZY2201	ZY2202	ZY2203	ZY2204	ZY2205	ZY2206	ZY2207
(wt.%)							
SiO ₂	58.18	59.44	59.13	58.24	56.26	56.01	55.57
TiO ₂	1.87	1.37	1.36	1.82	2.01	1.87	2.05
Al ₂ O ₃	14.38	14.37	14.24	14.11	14.18	15.00	14.41
TFe ₂ O ₃	10.38	9.04	9.17	10.00	10.35	10.18	10.50
MnO	0.15	0.14	0.14	0.14	0.17	0.14	0.15
MgO	2.73	2.81	2.96	2.59	2.70	2.92	2.94
CaO	5.85	5.29	5.33	5.60	5.61	6.06	5.81
Na ₂ O	2.76	2.85	2.87	2.79	2.56	2.60	2.56
K ₂ O	2.98	3.15	3.16	3.11	3.21	2.97	3.01
P ₂ O ₅	0.71	0.46	0.45	0.65	0.73	0.68	0.76
LOI	0.48	1.31	0.67	0.36	1.53	1.60	1.67
Total	100.47	100.23	99.48	99.41	99.31	100.03	99.43
(ppm)							
Li	11.2	19.8	19.9	14.8	18.6	20.7	18.2
Be	2.66	2.80	2.76	2.94	3.06	2.70	2.97
Sc	22.7	20.1	20.4	23.3	24.3	24.0	23.8
V	163	141	147	168	179	165	164
Cr	72.1	91.3	101.3	69.5	68.6	78.6	83.5
Ni	21.3	22.3	24.0	20.7	19.2	20.2	21.6
Cu	20.8	19.8	19.9	20.9	27.0	22.2	23.3
Zn	131	128	122	133	148	139	141
Ga	21.9	21.9	21.8	22.9	23.3	23.8	22.7
Rb	80.3	95.2	97.8	88.4	88.0	89.5	88.9
Sr	412	374	384	406	403	542	490
Y	47.5	44.4	43.8	48.4	49.3	44.8	46.7
Zr	402	478	474	435	428	400	407
Nb	20.2	21.2	21.0	21.2	22.7	20.3	21.8
Cs	0.60	0.77	0.74	0.95	2.98	3.63	4.44
Ba	1543	1515	1504	1544	1814	1714	1737
La	72.2	79.0	79.5	75.0	77.3	71.7	75.2
Ce	149	161	161	154	163	150	159
Pr	17.6	18.3	18.1	18.2	19.4	18.0	18.9
Nd	72.3	71.2	70.9	73.2	80.0	72.9	77.1
Sm	12.7	12.1	12.0	12.7	14.0	12.8	13.4
Eu	2.63	2.21	2.18	2.59	2.93	2.78	2.87
Gd	12.1	11.2	11.2	12.1	13.0	11.7	12.5
Tb	1.53	1.39	1.40	1.51	1.63	1.47	1.56
Dy	8.99	8.32	8.11	8.92	9.50	8.53	9.00
Ho	1.67	1.54	1.53	1.67	1.75	1.53	1.65
Er	4.97	4.56	4.54	4.95	5.09	4.55	4.87
Tm	0.62	0.55	0.55	0.60	0.63	0.55	0.58

Yb	4.26	3.79	3.84	4.18	4.33	3.82	3.99
Lu	0.61	0.55	0.56	0.60	0.63	0.55	0.58
Hf	7.97	9.09	9.15	8.20	8.46	7.59	7.98
Ta	1.03	0.98	0.99	1.01	1.10	0.96	1.07
Pb	16.4	21.2	18.0	16.3	18.9	15.2	14.2
Th	4.28	6.43	6.71	4.27	3.87	3.22	3.55
U	0.70	0.98	0.88	0.71	0.75	0.61	0.68
K ₂ O/Na ₂ O	1.08	1.11	1.10	1.11	1.25	1.14	1.18
K ₂ O+Na ₂ O (Wt.%)	5.74	6.00	6.03	5.90	5.77	5.57	5.57
Mg#	34.5	38.3	39.2	34.1	34.3	36.5	35.9
A/CNK	0.78	0.81	0.80	0.78	0.79	0.81	0.80
A/NK	1.85	1.77	1.75	1.77	1.84	2.00	1.93
ΣREE	361.5	375.8	375.1	370.4	393.2	361.2	381.3
Eu/Eu*	0.64	0.57	0.57	0.63	0.65	0.68	0.66
(La/Yb) _N	12.2	15.0	14.8	12.9	12.8	13.5	13.5

1280 Mg[#]=(MgO+FeO_{total})/MgO×100

1281 Eu/Eu^{*}=2Eu_N/(Sm_N+Gd_N); (La/Yb)_N=chondrite-normalized La/Yb ratio

1282

Table 2 Whole-rock Sr isotopic compositions of the late Paleoproterozoic diorites in the NCC

Sample	Age (Ma)	Rb (ppm)	Sr (ppm)	Rb/Sr	$^{87}\text{Rb}/^{86}\text{Sr}$	$^{87}\text{Sr}/^{86}\text{Sr}$	$\pm 2\text{SE}$	$^{87}\text{Sr}/^{86}\text{Sr}$ (t)	Error (abs.)	Data source
Jiguanshan diorite										
ZY2201	1780	80.3	412	0.20	0.5648	0.71931	0.000010	0.70485	0.00 077	This study
ZY2202	1780	95.2	374	0.25	0.7371	0.72471	0.000012	0.70584	0.00 099	
ZY2203	1780	97.8	384	0.25	0.7377	0.72434	0.000011	0.70546	0.00 099	
ZY2204	1780	88.4	406	0.22	0.6307	0.72111	0.000011	0.70496	0.00 085	
ZY2205	1780	88.0	403	0.22	0.6334	0.71856	0.000011	0.70235	0.00 086	
ZY2206	1780	89.5	542	0.17	0.4780	0.71518	0.000011	0.70294	0.00 066	
ZY2207	1780	88.9	490	0.18	0.5252	0.71542	0.000013	0.70198	0.00 072	
Wafang diorite										
WF1307-3	1780	107.0	389	0.28	0.7969	0.72131	0.000013	0.70091	0.00 106	Wang et al. (2016)
WF1307-4	1780	109.0	400	0.27	0.7895	0.72144	0.000014	0.70123	0.00 105	
WF1307-5	1780	84.0	411	0.20	0.5921	0.72024	0.000016	0.70508	0.00 080	
WF1307-8	1780	113.0	343	0.33	0.9548	0.72479	0.000016	0.70035	0.00 127	
WF1307-9	1780	110.0	373	0.29	0.8545	0.72236	0.000014	0.70048	0.00 114	
Shizhaigou diorite										
Ln-1	1780	103.7	272	0.38	1.1040	0.72874	0.000012	0.70048	0.00 146	Cui et al. (2011)
Ln-2	1780	101.5	322	0.31	0.9125	0.72868	0.000015	0.70532	0.00 121	
Ln-3	1780	136.4	200	0.68	1.9758	0.72509	0.00001	0.67452	0.00 259	
Ln-4	1780	116.6	295	0.40	1.1479	0.73149	0.000015	0.70210	0.00 152	
Ln-5	1780	112.5	300	0.38	1.0885	0.72997	0.000014	0.70211	0.00 144	
E-W Group dyke										
02SX001	1780	154.8	470	0.33	0.9542	0.72970	0.000014	0.70528	0.00 127	Peng et al. (2007)
02SX007	1780	81.2	450	0.18	0.5231	0.71858	0.000014	0.70519	0.00 072	
03LF01	1780	74.4	449	0.17	0.4801	0.71619	0.000013	0.70390	0.00 066	
03FS04	1780	131.8	229	0.58	1.6748	0.74399	0.000012	0.70112	0.00	

03FS07	1780	106.0	539	0.20	0.5699	0.71852	0.000013	0.70393	220 0.00 078
Weight mean value						0.70519	0.00 031	(n=8, calculated by IsoplotR)	

1284 $(^{87}\text{Sr}/^{86}\text{Sr})_s = (^{87}\text{Sr}/^{86}\text{Sr})_0 + (^{87}\text{Rb}/^{86}\text{Sr})_s \times (e^{\lambda t} - 1)$

1285 $\lambda_{^{87}\text{Rb}} = 1.42 \times 10^{-11}/\text{a}^{-1}$

1286 Error of initial ratio is calculated from the measurement error of the isotope ratio, the estimated
1287 concentration error and the age error. The decay constant is considered to be a fixed value.

1288 $\sigma_{\text{Sr}(t)}$ is mean-square deviation of $(^{87}\text{Sr}/^{86}\text{Sr})_t$

1289 σ_{Rb} is mean-square deviation of $(^{87}\text{Rb}/^{86}\text{Sr})_s$

1290 σ_t is mean-square deviation of age

$$1291 \sigma_{\text{Sr}(t)} = \sqrt{\sigma_{\text{Sr}}^2 + \sigma_{\text{Rb}}^2 (e^{\lambda t} - 1)^2 + \sigma_t^2 (\lambda e^{\lambda t} (\frac{^{87}\text{Rb}}{^{86}\text{Sr}}))^2}$$

1292

Table 3 Whole-rock Nd isotopic compositions of the late Paleoproterozoic diorites in the NCC

Sample	Age (Ma)	Nd (ppm)	Sm (ppm)	$^{147}\text{Sm}/^{144}\text{Nd}$	$^{143}\text{Nd}/^{144}\text{Nd}$	Error (2s)	$^{143}\text{Nd}/^{144}\text{Nd(t)}$
Jiguanshan diorite							
ZY2201	1780	72.3	12.7	0.1063	0.511238	0.000007	0.509994
ZY2202	1780	71.2	12.1	0.1029	0.511129	0.000008	0.509924
ZY2203	1780	70.9	12.0	0.1022	0.511131	0.000005	0.509934
ZY2204	1780	73.2	12.7	0.1049	0.511240	0.000007	0.510011
ZY2205	1780	80.0	14.0	0.1058	0.511329	0.000007	0.510090
ZY2206	1780	72.9	12.8	0.1058	0.511317	0.000005	0.510078
ZY2207	1780	77.1	13.4	0.1054	0.511320	0.000006	0.510086
E-W Group dyke							
02SX001	1780	113	20.3	0.1084	0.511287	0.000009	0.510018
02SX007	1780	62.6	11.3	0.1093	0.511285	0.000010	0.510005
03LF01	1780	45.1	8.36	0.1120	0.511358	0.000017	0.510047
03FS04	1780	102	17.5	0.1039	0.511270	0.000010	0.510053
03FS07	1780	62.7	11.1	0.1068	0.511297	0.000013	0.510047
Shizhaigou diorite							
Ln-1	1780	69.0	12.3	0.1075	0.511280	0.000012	0.510021
Ln-2	1780	66.4	11.7	0.1065	0.511270	0.000011	0.510023
Ln-3	1780	61.9	11.2	0.1090	0.511280	0.000011	0.510003
Ln-4	1780	71.1	12.6	0.1072	0.511260	0.000011	0.510005
Ln-5	1780	69.4	12.3	0.1072	0.511260	0.000012	0.510005
Wafang diorite							
WF1307-3	1780	78.4	13.7	0.1056	0.511169	0.000008	0.509953
WF1307-4	1780	78.5	14.1	0.1086	0.511215	0.000008	0.509965
WF1307-5	1780	75.9	13.7	0.1091	0.511192	0.000008	0.509936
WF1307-8	1780	77.6	13.4	0.1044	0.511039	0.000007	0.509837
WF1307-9	1780	77.5	13.9	0.1084	0.511193	0.000005	0.509945
Gushicun diorite							
20XRδ-1	1780	58.0	10.9	0.1134	0.511327	0.000004	0.509999
20XRδ-3	1780	63.3	11.7	0.1118	0.511334	0.000006	0.510025
20XRδ-4	1780	59.1	10.9	0.1118	0.511341	0.000006	0.510032
20XRδ-5	1780	53.1	9.9	0.1122	0.511354	0.000006	0.510041

The Muzhijie
diorites

20δPt2-1	1780	63.5	11.5	0.1090	0.511297	0.000004	0.510021
20δPt2-3	1780	64.2	11.7	0.1100	0.511300	0.000004	0.510012
20δPt2-5	1780	66.4	12.3	0.1122	0.511295	0.000007	0.509982
20δPt2-7	1780	72.1	13.1	0.1101	0.511297	0.000008	0.510007
20δPt2-9	1780	54.2	9.6	0.1076	0.511181	0.000006	0.509922
20δPt2-11	1780	64.5	11.4	0.1073	0.511199	0.000006	0.509943
20δPt2-13	1780	62.9	11.2	0.1076	0.511196	0.000008	0.509937
20δPt2-16	1780	67.9	12.3	0.1098	0.511270	0.000007	0.509984

Fudian diorite

20XRSC-1	1780	65.8	12.1	0.1110	0.511309	0.000006	0.510009
20XRSC-2	1780	67.1	12.3	0.1111	0.511315	0.000006	0.510014
20XRSC-3	1780	69.5	12.8	0.1113	0.511314	0.000004	0.510011
20XRSC-4	1780	67.5	12.5	0.1117	0.511311	0.000007	0.510002
20XRSC-5	1780	70.1	12.9	0.1111	0.511311	0.000006	0.510010
20XRSC-6	1780	68.9	12.7	0.1112	0.511324	0.000005	0.510022
20XRSC-8	1780	71.7	12.9	0.1089	0.511331	0.000006	0.510056
20XRSC-9	1780	76.6	13.9	0.1096	0.511325	0.000005	0.510042

Weight mean value

1294

1295

Error (abs.)	$\varepsilon_{\text{Nd}}(t)$	Error (ε_{Nd})	T_{DM2} (Ga)	Data source
0.000063	-6.69	1.24	2.83	
0.000061	-8.04	1.20	2.94	
0.000060	-7.85	1.19	2.93	
0.000062	-6.35	1.22	2.80	This study
0.000063	-4.80	1.23	2.68	
0.000063	-5.03	1.23	2.70	
0.000062	-4.88	1.22	2.68	
0.000065	-6.21	1.27	2.79	
0.000065	-6.47	1.28	2.81	
0.000068	-5.64	1.34	2.75	Peng et al. (2007)
0.000062	-5.53	1.22	2.74	
0.000064	-5.65	1.26	2.75	
0.000065	-6.15	1.26	2.79	
0.000064	-6.10	1.25	2.78	
0.000065	-6.50	1.28	2.82	Cui et al. (2011)
0.000064	-6.46	1.26	2.81	
0.000064	-6.46	1.26	2.81	
0.000062	-7.90	1.23	2.93	
0.000063	-7.67	1.26	2.91	
0.000064	-8.24	1.27	2.96	Wang et al. (2016)
0.000061	-10.2	1.21	3.11	
0.000063	-8.07	1.26	2.94	
0.000067	-6.58	1.31	2.82	
0.000066	-6.08	1.30	2.78	Ma et al. (2023a)
0.000066	-5.94	1.30	2.77	
0.000066	-5.77	1.30	2.76	
0.000064	-6.15	1.26	2.79	Ma et al. (2023b)

0.000065	-6.33	1.27	2.80
0.000067	-6.92	1.30	2.85
0.000065	-6.42	1.28	2.81
0.000064	-8.09	1.25	2.95
0.000064	-7.69	1.25	2.91
0.000064	-7.80	1.25	2.92
0.000065	-6.87	1.28	2.85

0.000066	-6.39	1.29	2.81
0.000066	-6.30	1.29	2.80
0.000066	-6.35	1.29	2.80
0.000066	-6.52	1.30	2.82
0.000066	-6.37	1.29	2.81
0.000066	-6.14	1.29	2.79
0.000065	-5.46	1.26	2.75
0.000065	-5.74	1.27	2.75

Ma et al. (2023b)

-6.51 0.20 (n = 41, calculated by IsoplotR)

1296 $(^{143}\text{Nd}/^{144}\text{Nd})_s = (^{143}\text{Nd}/^{144}\text{Nd})_0 + (^{147}\text{Sm}/^{144}\text{Nd})_s \times (e^{\lambda t} - 1)$

1297 $\varepsilon_{\text{Nd}}(t) = [(^{143}\text{Nd}/^{144}\text{Nd})_i / (^{143}\text{Nd}/^{144}\text{Nd})_{\text{CHUR}(t)} - 1] \times 10000$

1298 $T_{\text{DM2}} = 1/\lambda \times \ln \{1 + [(^{143}\text{Nd}/^{144}\text{Nd})_{\text{DM}} - (^{143}\text{Nd}/^{144}\text{Nd})_s + ((^{147}\text{Sm}/^{144}\text{Nd})_s - (^{147}\text{Sm}/^{144}\text{Nd})_{\text{CC}}) \times (e^{\lambda t} - 1)]\}$

1299 $\varepsilon_{\text{Nd}}(t) = [(^{143}\text{Nd}/^{144}\text{Nd})_i / (^{143}\text{Nd}/^{144}\text{Nd})_{\text{CHUR}(t)} - 1] \times 10000 / ((^{147}\text{Sm}/^{144}\text{Nd})_{\text{DM}} - (^{147}\text{Sm}/^{144}\text{Nd})_{\text{CC}})$

1300 $\lambda_{^{147}\text{Sm}} = 0.654 \times 10^{-11}/\text{a}^{-1}$

1301 $^{143}\text{Nd}/^{144}\text{Nd})_{\text{DM}} = 0.51315$

1302 $^{147}\text{Sm}/^{144}\text{Nd})_{\text{DM}} = 0.2137$

1303 $^{147}\text{Sm}/^{144}\text{Nd})_{\text{CC}} = 0.12$

1304 Error of initial ratio is calculated from the measurement error of the isotope ratio, the estimated
1305 concentration error and the age error. The decay constant is considered to be a fixed value.

1306 $\sigma_{\text{Nd}(t)}$ is mean-square deviation of $(^{143}\text{Nd}/^{144}\text{Nd})_i$

1307 σ_{Sm} is mean-square deviation of $(^{143}\text{Sm}/^{144}\text{Nd})_s$

1308 σ_t is mean-square deviation of age

$$\sigma_{\text{Nd}(t)} = \sqrt{\sigma_{\text{Nd}}^2 + \sigma_{\text{Sm}}^2 (e^{\lambda t} - 1)^2 + \sigma_t^2 (\lambda e^{\lambda t} (\frac{^{147}\text{Sm}}{^{144}\text{Nd}}))^2}$$

1309

1310

1311

Table 4 Whole-rock Pb isotopic compositions of the Jiguanshan diorite

Spon.no	U (ppm)	Th (ppm)	Pb (ppm)	$^{206}\text{Pb}/^{204}\text{Pb}$	$\pm 2\text{SE}$	$^{207}\text{Pb}/^{204}\text{Pb}$	$\pm 2\text{SE}$
ZY2201	0.70	4.28	16.38	15.867	0.0005	15.189	0.0005
ZY2202	0.98	6.43	21.20	16.167	0.0008	15.243	0.0009
ZY2203	0.88	6.71	18.03	15.882	0.0006	15.182	0.0006
ZY2204	0.71	4.27	16.29	16.097	0.0010	15.225	0.0009
ZY2205	0.75	3.87	18.90	15.832	0.0007	15.179	0.0006
ZY2206	0.61	3.22	15.22	15.914	0.0010	15.170	0.0010
ZY2207	0.68	3.55	14.22	16.036	0.0008	15.199	0.0007

1312

1313

$^{208}\text{Pb}/^{204}\text{Pb}$	$\pm 2\text{SE}$	$^{206}\text{Pb}/^{204}\text{Pb}$	$^{207}\text{Pb}/^{204}\text{Pb}$	$^{208}\text{Pb}/^{204}\text{Pb}$	$^{238}\text{U}/^{204}\text{Pb}$	$^{232}\text{Th}/^{204}\text{Pb}$	$^{232}\text{Th}/^{238}\text{U}$
		initial	initial	initial	μ	ω	
36.502	0.0014	15.063	15.103	35.027	2.6	16.0	6.3
37.126	0.0022	15.295	15.150	35.392	2.8	18.8	6.8
36.494	0.0013	14.965	15.084	34.398	2.9	22.8	7.8
37.324	0.0023	15.271	15.137	35.825	2.6	16.3	6.2
36.046	0.0016	15.095	15.100	34.901	2.3	12.4	5.3
36.124	0.0024	15.164	15.090	34.939	2.4	12.9	5.4
36.338	0.0016	15.136	15.103	34.931	2.9	15.3	5.4

1314 Initial Pb isotopic ratios are calculated back to 1780 Ma.

1315

1316 **Supplementary material/Appendix:**

1317 **Table S1** Zircon U–Pb isotopic data for the Jiguanshan diorite obtained by the LA-ICP-MS
1318 technique

1319 **Table S2** Zircon trace element data for the Jiguanshan diorite obtained by the LA-ICP-MS
1320 technique

1321

1322

1323